CANCER

Red blood cell–hitchhiking fluorescent probe to promote intraoperative diagnosis of human ovarian tumor

Yijing Lin[1]†, Ke Li[1]†, Yue Ding[1], Seok Theng Chiang[2], Jingzhou Xia[3], Haonan Wang[4], Huafeng Wang[5], Xiangzhao Ai[2]*, Weiwei Feng[1]*

Ovarian cancer is the deadliest gynecological malignancy. The fluorescence-guided surgery technique provides a real-time visualization of the desired regions to guide the tumor resection. However, the fluorescent probes used in clinics suffer from the limited selectivity of ovarian tumors and short blood circulation half-lives. Here, we design an activatable trident-like fluorescent peptide probe (RMN) to bind with the ovarian tumor-overexpressed N-cadherin and respond to the matrix metalloproteinases (MMPs). Upon intravenous administration, the RMN initially hitchhikes on the red blood cell (RBC) surface with prolonged circulation half-lives. When arriving at the tumor regions, the peptide sequence is cleaved by the tumor-secreted MMPs to recover the fluorescent signals. The released "spears" containing N-cadherin–targeting moiety and fluorophore can specifically recognize the ovarian tumor cells, thereby facilitating the visualization of primary or metastatic tumor regions. Overall, this study highlights the potential of RBC-hitchhiking fluorescent probes in advancing the intraoperative diagnosis of human ovarian tumor tissues during the fluorescence-guided surgery process in clinics.

INTRODUCTION

Ovarian cancer, known as "the silent killer," is the deadliest gynecological malignancy. It caused an estimated 0.324 million new cases and 0.207 million deaths globally in 2022 (*1*–*3*). More than 70% of patients with ovarian cancer are diagnosed in the advanced tumor stages (III or IV), with a 5-year survival rate of less than 30% (*4*–*6*). Now, surgery remains an indispensable first-line treatment strategy for patients with ovarian cancer (*7*). Multiple preoperative imaging techniques, such as computed tomography (CT), magnetic resonance imaging (MRI), and positron emission tomography (PET), have been widely applied to determine the specific locations of tumors (*8*–*10*). However, in the surgical processes, the tumor removal efficiency still highly relies on the gynecologic surgeons' clinical experience, such as visual inspection and manual palpation, to differentiate tumor tissue from surrounding tissues (*11*). This reliance potentially results in either the excessive removal of adjacent normal tissues or the incomplete tumor resection to cause ovarian cancer recurrence (*12*). Although intraoperative frozen section analysis (IFSA) and intraoperative CT or MRI systems have been developed to assist the surgeons in visualizing tumor regions and metastatic foci during surgery, these techniques present undesired limitations in clinical settings (*13*, *14*). For example, IFSA has insufficient sensitivity to accurately diagnose tumor-positive margins and is a time-consuming process to increase the operative or anesthesia-related risks, whereas intraoperative CT/MRI requires sophisticated equipment, substantial physical space, and expensive costs (*15*, *16*). Hence, emerging approaches for intraoperative diagnosis are demanded to visualize tumor regions during surgery, thus greatly improving ovarian tumor resection efficiency and benefiting the overall survival rates of patients with cancer.

In recent years, the fluorescence-guided surgery (FGS) technique has attracted much attention in clinics to provide a real-time fluorescence image of the tumor regions and guide the tumor surgical resection (*17*–*27*). FGS has unique advantages for intraoperative tumor diagnosis, including high sensitivity with excellent spatiotemporal resolution, rapid or real-time tumor visualization, and low-cost or portable equipment (*28*–*31*). Various fluorescent probes, including indocyanine green, methylene blue, fluorescein sodium, and 5-aminolevulinic acid, have been developed to light up the tumor tissues during surgery due to an enhanced permeability and retention effect (*32*). However, their clinical applications are extremely limited by the nonspecific imaging of normal tissues, especially in the operation regions contaminated by the fluorescent dyes circulating in the blood vessels (*33*, *34*). Recently, specific fluorescent probes have also been designed by conjugating a fluorophore with the tumor-targeting ligands to recognize the overexpressed receptors on the tumor cell surface, such as folate receptor, glutamine transporter, and epidermal growth factor receptor (*35*–*40*). Nevertheless, these fluorescent probes emit fluorescence continuously upon injection in vivo, regardless of their binding with targeted receptors, resulting in higher background and an insufficient signal-to-noise ratio (*41*). They commonly exhibit a short blood circulation time within several minutes due to the rapid hepatic and renal elimination of small molecules upon systemic administration (*42*, *43*). These critical limitations lead to a demand for imaging probes at a higher dose and frequent injection during the surgery in several hours, which may raise the potential risk of systemic toxicity and increasing costs. Therefore, innovative fluorescent probes with prolonged blood circulation time and specific signal activation in tumor regions are highly desired to improve the ovarian tumor intraoperative diagnosis efficiency.

[1]Department of Gynecology and Obstetrics, Ruijin Hospital, Shanghai Jiao Tong University School of Medicine, Shanghai 200025, China. [2]Department of Bioengineering, School of Life Sciences and Biotechnology, Shanghai Jiao Tong University, Shanghai 200240, China. [3]School of Design, Shanghai Jiao Tong University, Shanghai 200240, China. [4]Department of Clinical Pharmacy, The First Affiliated Hospital, Zhejiang University School of Medicine, Zhejiang University, Hangzhou 310003, China. [5]Department of Pathology, Ruijin Hospital, Shanghai Jiao Tong University School of Medicine, Shanghai 200025, China.
*Corresponding author. Email: xzai@sjtu.edu.cn (X.A.); fww12066@rjh.com.cn (W.F.)
†These authors contributed equally to this work.

Natural red blood cells (RBCs) serve as ideal carriers for small molecules due to their long circulatory life span (~120 days in humans) and low immunogenicity in vivo (*44*–*60*). Meanwhile, the tumor tissues usually have abundant vasculature and abnormal hyperpermeability, resulting in the increased RBC concentration in the tumor regions (*61*). Inspired by the unique properties of RBCs, we hypothesize that the RBC-hitchhiking fluorescent probes have prolonged blood circulation half-lives and enhanced ovarian tumor targeting capabilities. Herein, we design a trident molecule, which contains three functional "spears" in the peptide backbone: (i) an N-cadherin–binding peptide to act as the ovarian tumor-targeting moiety; (ii) a fluorophore; and (iii) a quencher, serving as a fluorescence resonance energy transfer (FRET) pair to minimize the undesired background in normal tissues (Fig. 1A). The "branch" of

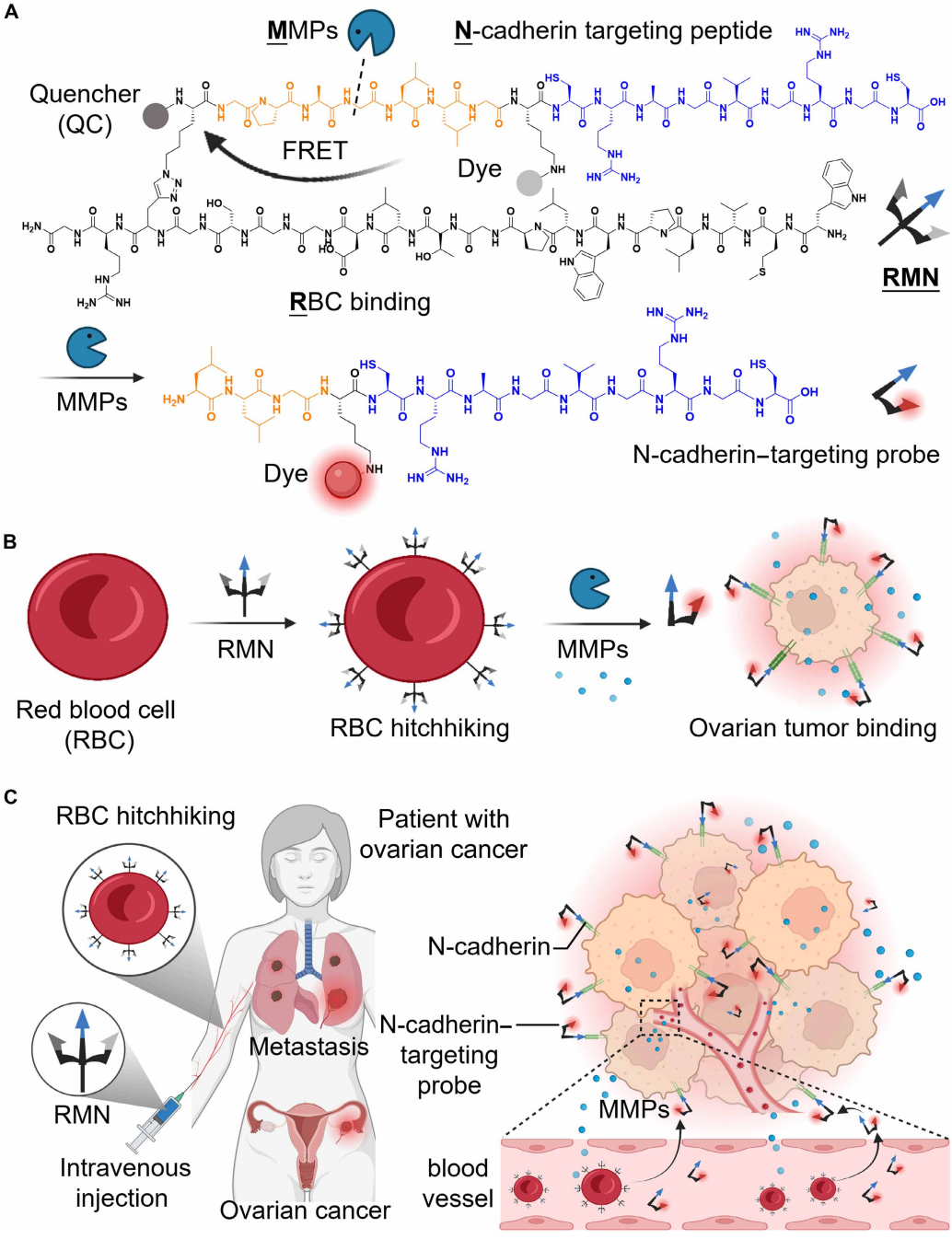

Fig. 1. RBC-hitchhiking trident-like fluorescent probe (RMN) for the diagnosis of ovarian tumor and metastatic foci. (**A**) Chemical structures of RMN. (**B** and **C**) Schematic illustration of RMN bind to RBC and response to MMPs for the tumor-specific intraoperative diagnosis in ovarian cancer. Created in BioRender. Lin, Y. (2025) https://BioRender.com/k1xh8m5.

quencher is constituted of an enzyme-responsive linker that can be cleaved by the ovarian tumor-overexpressed matrix metalloproteinases (MMPs). The "handle" of the trident molecule is made of an RBC-hitchhiking peptide to bind with the major transmembrane protein glycophorin A on the surface of erythrocytes. Upon systematic administration, the trident molecule (RBC–MMP2/9–N-cadherin, denoted "RMN") initially hitchhikes on RBCs with prolonged circulation time in the blood. When arriving at the ovarian tumor regions, the secreted MMPs from the tumor microenvironment can effectively cleave the branch peptide sequence, thus selectively recovering the emission of fluorophore in the tumor regions. The released two functional spears containing targeting peptide moiety and fluorophore can specifically recognize the surrounding N-cadherin–overexpressed ovarian tumor cells, thereby facilitating the visualization of tumor regions during the surgery process (Fig. 1, B and C). Our results demonstrate that the trident-like fluorescent probe can effectively recognize the subcutaneous and metastatic foci of ovarian tumors in the nude mice upon intravenous administration, as well as the human ovarian tumor tissues for intraoperative diagnosis in clinical settings.

RESULTS

Overexpression of N-cadherin in human ovarian tumors

We first determined the expression levels of N-cadherin, a major adhesion molecule involved in tumor progression and metastasis in the human patients with ovarian cancer (*62*, *63*). In this study, both tumor and normal ovarian tissues were collected from the Chinese patients after surgery in Ruijin hospitals (Fig. 2A and table S1 and S2) and further analyzed by immunohistochemistry using an anti–N-cadherin antibody. As shown in Fig. 2B, the brown precipitates were observed in the sections of ovarian tumor tissues rather than the normal ovarian tissues. The average histochemical scoring (*H*-score) value of tumor tissues (7.00 ± 5.37, 60 cases) was significantly higher

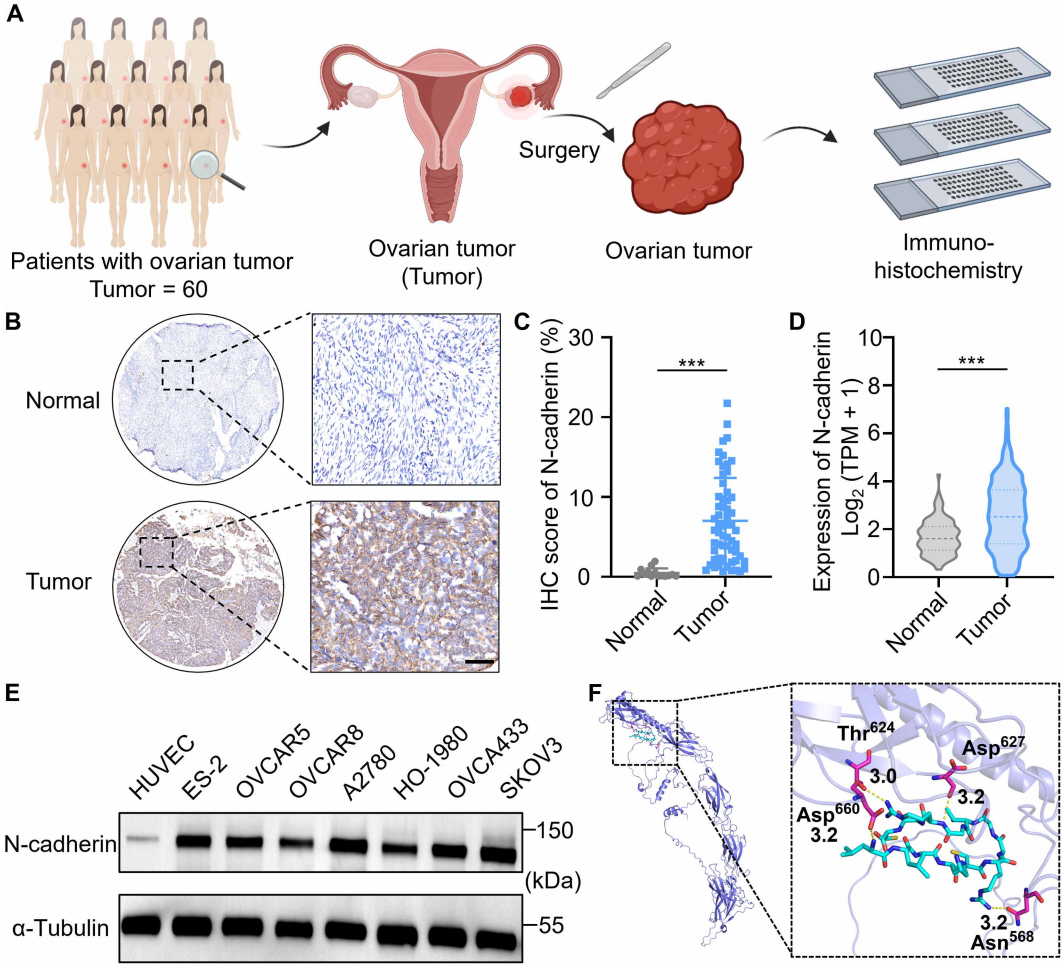

Fig. 2. N-cadherin overexpression in human ovarian tumor tissues and tumor cells. (**A**) Schematic illustration of N-cadherin analysis in the samples from ovarian tumor patients. Created in BioRender. Lin, Y. (2025) https://BioRender.com/n6w6wm6. (**B**) Representative immunohistochemistry of N-cadherin expression in human ovarian tumor tissues. Scale bar, 50 μm. (**C**) Quantification of N-cadherin expression using histochemical score (*H*-score) in ovarian tumor tissues (60 cases) and normal ovarian tissues (14 cases). (**D**) Analysis of N-cadherin expression in ovarian tumors ($n = 381$) and normal ovarian tissues ($n = 88$) from the TCGA and GTEx databases. TPM, transcripts per million. (**E**) Western blot analysis of N-cadherin expression in human ovarian tumor cells (ES-2, OVCAR5, OVCAR8, A2780, HO-1980, OVCA433, and SKOV3) and normal cells (HUVECs). (**F**) Molecular docking of human N-cadherin protein (violet) and targeting peptide (cyan). The binding sites of N-cadherin are colored in magenta. Hydrogen bonds (×Å) and distance are depicted as yellow dashed lines.

than that of normal tissues (0.49 ± 0.57, 14 cases), implying the overexpression of N-cadherin in human patients with ovarian cancer (Fig. 2C). The N-cadherin expression levels in the tumor and normal tissues of human ovaries were also investigated in the database of The Cancer Genome Atlas (TCGA; www.cancer.gov/tcga) and Genotype-Tissue Expression (GTEx; www.gtexportal.org), including the data from 381 cases of ovarian tumor tissues and 88 cases of normal ovarian tissues globally. Demographic information indicated that most patients with high expression of N-cadherin are Caucasians (white people), with the onset time ranging from 41 to 60 years old in the advanced stage III of cancer (fig. S1). Moreover, bioinformatics analyses suggested that the expression of N-cadherin was markedly higher in ovarian tumor tissues than in normal tissues (Fig. 2D), and the Kaplan-Meier curve showed that N-cadherin in ovarian cancer had no obvious effect on patient survival (fig. S2). We further examined the N-cadherin levels in different subtypes of human ovarian cancer cell lines, including high-grade serous ovarian cancer (HGSOC; e.g., SKOV3, HO-8910, OVCAR5, OVCAR8, and OVCA433 cells), clear cell ovarian cancer (CCOC; e.g., ES-2 cells), and endometrioid ovarian cancer (e.g., A2780 cells), respectively. Healthy human umbilical vein endothelial cells (HUVECs) were used as a control group. As shown in Fig. 2E, the Western blot results revealed the highest levels of N-cadherin in the SKOV3 cell line compared to other control groups. The overexpression of N-cadherin in ovarian cancer inspired us to explore the N-cadherin–targeting strategies for ovarian tumor imaging in preclinical studies. A target peptide, CRAGVGRGC, has been selected using phage-display techniques to specifically identify the overexpressed N-cadherin in both murine and human breast tumor cells but has not been reported to recognize the N-cadherin in human ovarian cancer (*64*). To evaluate their binding affinity, we performed the molecular docking analysis by AlphaFold and found the formation of suitable steric complementarity between the target peptide and human N-cadherin, especially for the hydrogen bonds between the peptide (e.g., guanidine groups) and amino acid residues of N-cadherin protein, including the threonine (Thr^{624}), asparagine (Asn^{568}), or aspartic acid (Asp^{660} and Asp^{627}) (Fig. 2F). The equilibrium dissociation constant (K_d) was further calculated as 2.84×10^{-5} M based on the molecular docking model. Together, these results suggested that the overexpressed N-cadherin protein may serve as a potential receptor for the targeted recognition of human ovarian tumor cells.

Preparation and responsiveness of RMN probe in vitro

We then prepared the N-cadherin–targeting RMN probe based on a standard 9-fluorenyl methoxycarbonyl (Fmoc)–based solid-phase peptide synthesis (SPPS) procedure (figs. S3 to S5). To achieve the fluorescent visualization of ovarian tumor cells in vitro, an MMP enzyme–cleavable peptide sequence (GPAG↓LLG) with a FRET pair [e.g., donor, fluorescein isothiocyanate (FITC); and quencher, Dabcyl] modification was conjugated with the N-cadherin–targeting peptide. An RBC-hitchhiking peptide (WMVLPWLPGTLD) was further conjugated with the N-cadherin–targeting probes by click chemistry and lastly purified by preparative high-performance liquid chromatography (HPLC). The purity and molecular weight of various fluorescent peptide probes were confirmed by liquid chromatography–mass spectrometry (LC-MS; fig. S6 and table S3). In this study, we first investigated the photophysical properties of the FITC/Dabcyl-modified RMN peptide probes (FITC/QC-RMN) in phosphate-buffered saline (PBS). A similar peptide probe without quencher (QC) modification (FITC-RMN) was used as a control group. As shown in Fig. 3A, the absorption peak (~490 nm) of FITC-RMN shifted to a broad absorption spectrum of FITC/QC-RMN centered on ~450 nm, and the emission spectrum of FITC-RMN at 520 nm was significantly eliminated upon Dabcyl modification, mainly attributable to the fluorescence quenching of FITC by the Dabcyl group as an efficient FRET acceptor. The FITC-RMN peptide probes also presented excellent photostability and time-dependent structural stability in various physiological buffers, including 1× PBS, 10% fetal bovine serum (FBS), and 10% serum in cell culture medium (fig. S7). To visualize the N-cadherin–binding capability in living cells, the FITC-RMN probe was incubated with N-cadherin–overexpressed SKOV3 cells for 30 min and examined by confocal microscopy. The imaging results revealed that the green fluorescence signal of FITC was colocalized with the red fluorescence of a cell membrane tracker, implying that the FITC-RMN peptide probe was mainly trapped on the plasma membrane of ovarian tumor cells (Fig. 3B). When the incubation time increased to 4 hours, the green fluorescence of FITC was mainly overlapped with the red fluorescence of the lysosome tracker, suggesting the time-dependent endocytosis of RMN probe in the lysosome (fig. S8). The binding capability of the FITC-RMN probe was also determined by flow cytometry analysis. As shown in Fig. 3C and fig. S9, the fluorescence intensity enhanced with the increasing of FITC-RMN concentrations, suggesting a dose-dependent manner of N-cadherin binding in SKOV3 cells. We also incubated the FITC-RMN probe with different kinds of human ovarian cancer cells (e.g., A2780, ES-2, OVCAR5, OVCA433, and SKOV3) and normal cells (HUVECs) for fluorescence detection. As shown in Fig. 3 (D and E), the green fluorescence signals of the FITC-RMN probe in SKOV3 cells were higher than those in other control groups, suggesting the feasibility of N-cadherin–targeted imaging in various human ovarian tumor cells. To further identify the tumor selectivity of the RMN peptide probe, we incubated it with the N-cadherin–positive breast cancer cells (MDA-MB-231 and BT549) and liver cancer cells (HCCLM3 and HUH-7) for fluorescence analysis. As shown in fig. S10, the fluorescence signals of the FITC-RMN probe in both breast and liver cancer cells were obviously lower than that in ovarian cancer cells but higher than the normal cells, demonstrating that the RMN probe had broad applicability for the diagnosis of multiple N-cadherin–positive tumors, especially for different kinds of human ovarian cancer cells.

Next, we investigated the responsiveness of the FITC/QC-RMN peptide probe in the ovarian tumor cells. Previous studies have demonstrated that both MMP-2 and MMP-9 enzymes were overexpressed in ovarian carcinomas (*65*). Specifically, MMP-2 promotes the degradation of fibronectin and vitronectin to generate proteolytic fragments that are involved in ovarian tumor metastasis. MMP-9 mainly degrades the type IV collagen and fibronectin, resulting in the activation of transforming growth factor–β to enable effective matrix penetration of tumor cells. Thus, MMP enzymes, especially MMP-2 and MMP-9, play important roles in human ovarian cancer progression and metastasis. In this study, we selected a reported peptide (GPAG↓LLG) that was known to be specifically cleaved between glycine (G) and leucine (L) by both overexpressed MMP-2 and MMP-9 in human ovarian tumor cells (*66*). The excessive RMN peptide probe was first incubated with activated MMP-2 or MMP-9 for 30 min in a 37°C incubator. After ultrafiltration to remove the MMPs protein, the peptide substrates were examined by LC-MS. As

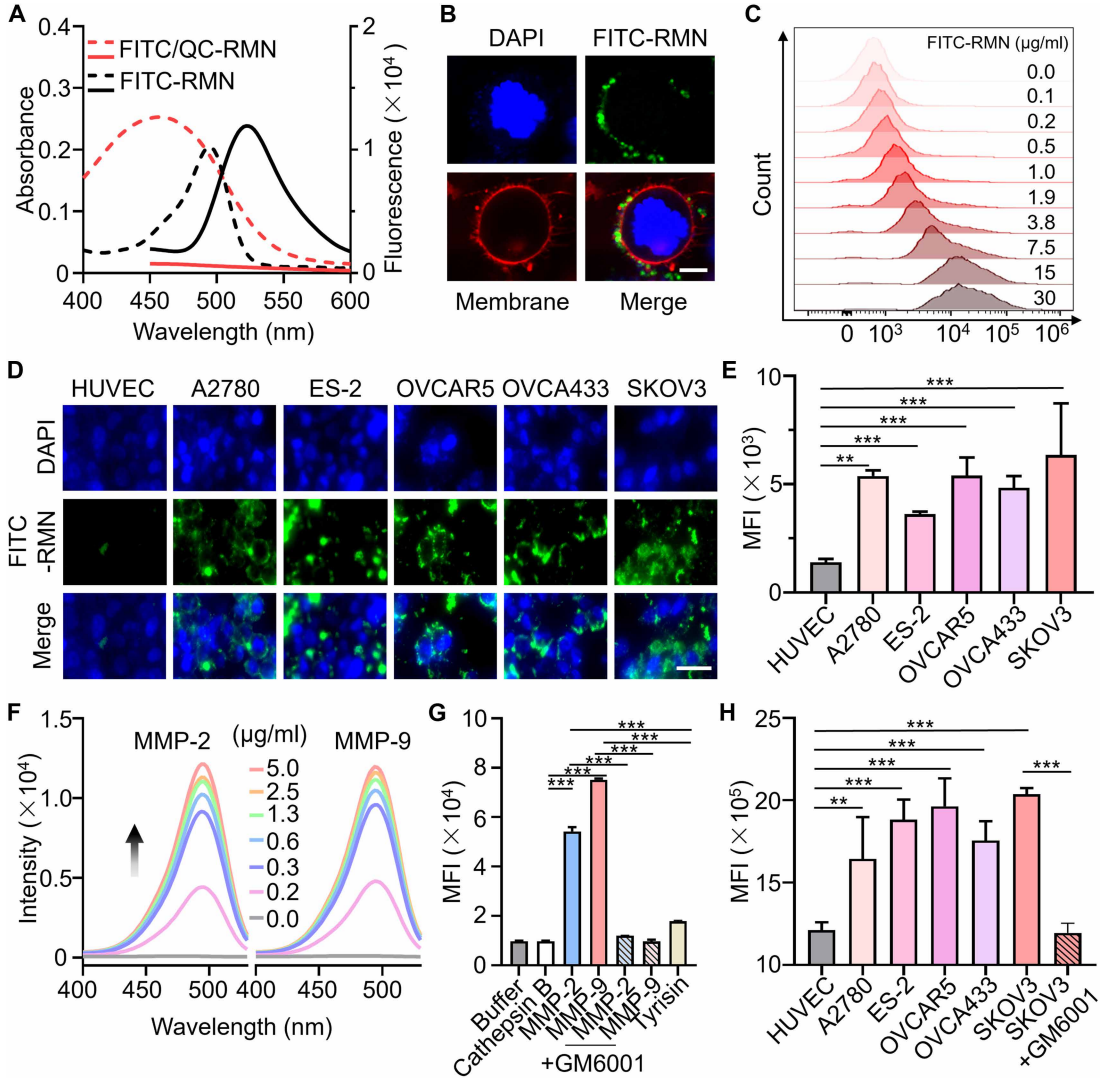

Fig. 3. RMN fluorescent probe recognizes and responds to human ovarian cells in vitro. (**A**) Absorbance (dashed lines) and fluorescence emission spectra (solid lines) of FITC/QC-RMN and FITC-RMN in PBS. (**B**) Confocal imaging of SKOV3 cells incubated with FITC-RMN for 30 min. Blue, DAPI [excitation/emission (Ex/Em), 350/460 nm]; green, FITC-RMN (Ex/Em, 488/525 nm); red, cell membrane tracker (Ex/Em, 645/665 nm). Scale bar, 10 μm. (**C**) Flow cytometry analysis of FITC-RMN probe (0 to 30 μg/ml) binding with SKOV3 cells. (**D**) Fluorescence images in human ovarian tumor cells (A2780, ES-2, OVCAR5, OVCA433, and SKOV3) and normal cells (HUVECs) incubated with FITC-RMN (30 μg/ml). Scale bar, 60 μm. (**E**) Mean fluorescence intensity (MFI) of HUVEC and human ovarian tumor cells (A2780, ES-2, OVCAR5, OVCA433, and SKOV3) after incubation with FITC-RMN fluorescent probe (30 μg/ml) for 30 min. (**F**) Responsiveness of FITC/QC-RMN probe (30 μg/ml) in the presence of activated MMP-2 and MMP-9 enzymes (5 μg/ml) for 30 min. (**G**) Selectivity study of FITC/QC-RMN upon the treatment of cathepsin B, trypsin, MMP-2, MMP-2 treated by GM6001 (50 μM), MMP-9, or MMP-9 treated by GM6001 (50 μM) at the same concentration (5 μg/ml), respectively. (**H**) MFI of FITC/QC-RMN probe (30 μg/ml) incubated with the culture medium of various human ovarian tumor cells (A2780, ES-2, OVCAR5, OVCA433, SKOV3, and SKOV3 treated by 100 μM GM6001) and normal cells (HUVECs) for 30 min.

shown in fig. S11, a new peak appeared at the same retention time (~10.4 min) upon MMP-2 and MMP-9 treatment. The molecular weight matched well with the N-cadherin–binding fragments upon cleavage between glycine and leucine, implying the specific substrate recognition of MMP enzymes (table S3). However, no obvious difference was observed for the retention time of the RMN probe (~11.2 min) in the absence and presence of cathepsin B, a tumor-overexpressed lysosomal cysteine protease primarily responsible for the degradation of intracellular proteins, suggesting the excellent specificity of RMN in response to MMP enzymes rather than others. Then, we optimized the incubation time and MMP enzyme concentrations at the same amounts of FITC/QC-RMN peptide probe. As shown in Fig. 3F and fig. S12, the fluorescence emission at ~500 nm of the FITC/QC-RMN probe was gradually enhanced with the increasing of MMP-2 or MMP-9 concentrations. The mean fluorescence intensity (MFI) of the FITC/QC-RMN peptide probe was also markedly increased and reached a plateau after 10 min of incubation (fig. S13), suggesting a dose-dependent and time-dependent manner in this MMP-responsive fluorescent probe. To evaluate its selectivity, the same concentrations of cathepsin B, trypsin (a serine proteinase to digest protein in healthy individuals), MMP-2, or MMP-9 were incubated with the same amounts of FITC/QC-RMN probe for fluorescence detection. As shown in Fig. 3G, we observed an elevated MFI in both MMP-2 and MMP-9 treated groups, while

no obvious difference was determined in the cathepsin B or trypsin treated groups when compared to the untreated group. In addition, the enhanced fluorescence signals of RMN upon MMP-2 and MMP-9 treatment were greatly inhibited by ilomastat (GM6001), a potent and broad-spectrum inhibitor of MMPs, suggesting the specificity of MMPs for RMN probe activation. To further assess the MMPs' activities in living cells, the concentrated culture media of various human ovarian tumor cells were incubated with the FITC/QC-RMN peptide probe, followed by the fluorescence analysis. As shown in Fig. 3H, the highest MFI values were determined in the EC-2, OVCAR5, and SKOV3 cells, mainly attributable to their extracellular secretion of a large amount of MMPs during the proliferation process, which also could be greatly inhibited by the GM6001. In addition, cell viability studies showed that the FITC/QC-RMN peptide probe had negligible cytotoxicity in the SKOV3 cells, as well as the normal cell lines such as HUVEC and murine macrophage (RAW264.7), indicating the excellent biosafety of the FITC/QC-RMN probe in vitro (fig. S14). Together, these results demonstrated that the biocompatible RMN peptide probe could effectively bind with the overexpressed N-cadherin and respond to the MMPs secreted from human ovarian tumor cells.

Prolonged circulation time of RBC-hitchhiking RMN probe in vivo

We further investigated the pharmacokinetic properties of the RMN probe. An RBC-hitchhiking peptide (ERY1, WMVLPWLPGTLD) was integrated into the peptide structure to recognize the glycophorin A protein on the RBC membrane. The K_d value was calculated to be 3.0×10^{-4} M based on the molecular docking model (fig. S15). To confirm the binding capability, RBCs were first incubated with the FITC-labeled RMN peptide probe and determined on the basis of the fluorescence signals of FITC on the RBC membrane. A similar peptide probe without ERY1 conjugation (MN) was used as a control group. Moreover, whole-blood samples from patients with ovarian cancer and tumor-bearing mice were also incubated with the MN or RMN probe to simulate their injection directly into the blood. As shown in Fig. 4A and fig. S16 and S17, the MFI and fluorescence imaging of RMN-treated RBCs exhibited a higher signal than the

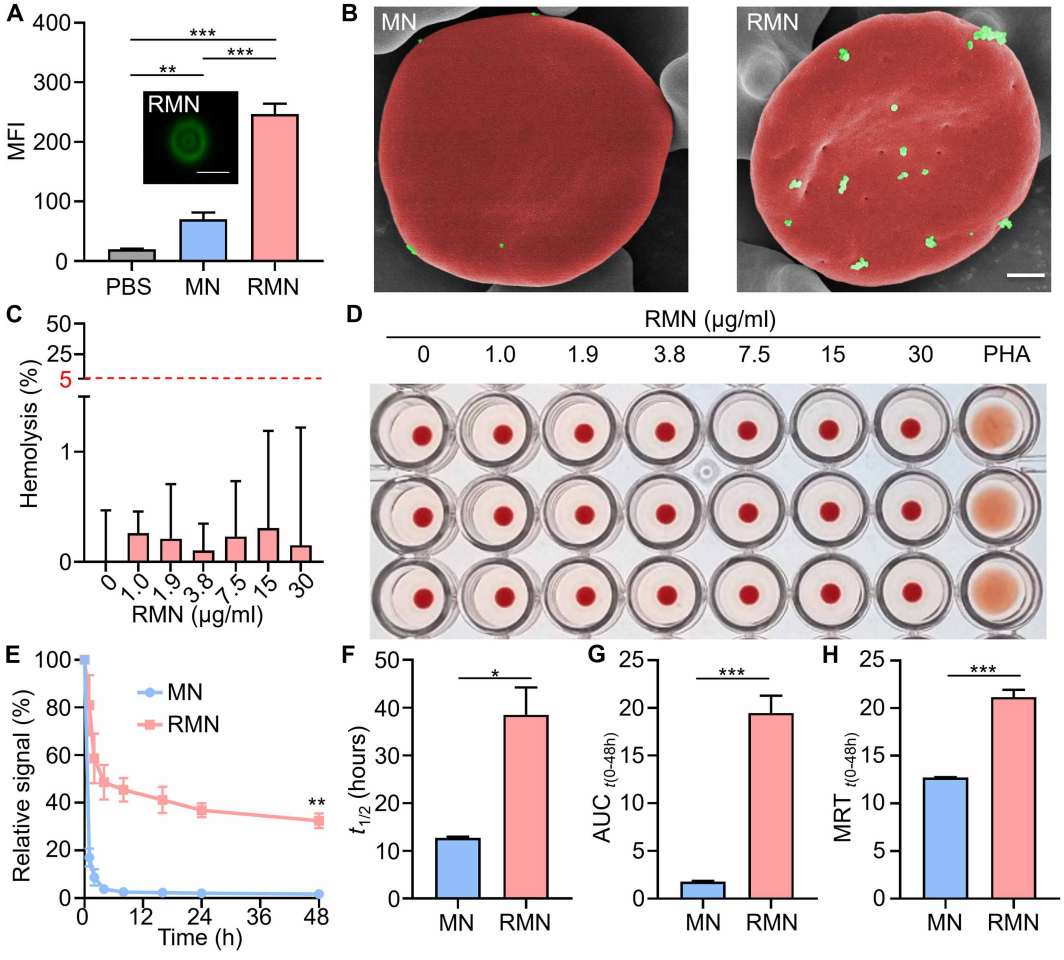

Fig. 4. Prolonged circulation time of RBC-hitchhiking RMN probe in vivo. (**A**) MFI of FITC-labeled RMN probe hitchhiking on RBCs' surface. Inset: Fluorescence image of RMN loaded on RBC surface. Scale bar, 10 μm. (**B**) Pseudocolored scanning electron microscopy (SEM) images of RBCs (red) incubated with FITC-labeled RMN or MN (green). Scale bar, 1 μm. (**C** and **D**) Quantification of hemolysis (C) and agglutination (D) levels in RBCs upon the treatment of FITC-labeled RMN probe at different concentrations (0 to 30 μg/ml). RBCs treated with phytohemagglutinin (PHA; 100 μg/ml) were used as a positive control. (**E** to **H**) Relative fluorescence signals (E), serum half-lives ($t_{1/2}$) (F), area under the curve [$AUC_{(0\text{-}48h)}$] (G) and mean residence time [$MRT_{(0\text{-}48h)}$] (H) of Cy5-labeled RMN or MN (0.15 mg/kg) upon intravenous injection in healthy mice. h, hours.

RBCs treated with MN or PBS in both murine and human blood samples, suggesting the strong hitchhiking capabilities of the RMN probe on the RBCs' surface. The average number of RMN that conjunct to erythrocytes was determined to be $(3.4 \pm 1.0) \times 10^6$/cell. Moreover, no obvious changes of fluorescence signals were determined on the RMN-treated RBCs at different time points during 24 hours, suggesting that the RMN peptide probe exhibited excellent stability on the RBC surface (fig. S18). Scanning electron microscopy (SEM) imaging further confirmed that more RMN peptide probe (green) was localized on the surface of RBCs (red) when compared to the MN group (Fig. 4B), attributable to the RBC-hitchhiking properties of the RMN probe rather than the nonspecific absorption on the RBCs surface. We further assessed the hemocompatibility of the RMN peptide probe on the basis of the hemolysis and agglutination assay. Hemolysis levels act as a major indicator to evaluate the potential damage of molecules on RBCs, which may induce undesired immune dysregulation and organ damage. In the hemolysis assay, varying concentrations of RMN probe were incubated with RBCs, followed by the detection of hemoglobin in the supernatant. As shown in Fig. 4C, negligible hemolysis (<1%) was observed on the RMN-loaded RBCs at all of the tested concentrations. In addition, RBC agglutination, which may cause vascular occlusion in the body, was also evaluated based on a gold-standard round-bottom-well assay in vitro. In this assay, the agglutinated RBCs form a large and diffused film, while nonagglutinated RBCs appear as a small red dot at the bottom of each well. Phytohemagglutinin (PHA) was usually selected as a positive control to cause 100% RBC agglutination. As shown in Fig. 4D, no obvious agglutination was observed in the RBCs upon the treatment of RMN peptide at a variety of concentrations. These results demonstrated that the RMN probe could effectively hitchhike on the RBCs' surface with excellent hemocompatibility.

Following the assessment of RBC-hitchhiking capability in vitro, we then investigated the pharmacokinetic profiles of the RMN peptide probe in vivo. To minimize the autofluorescence background in living animals, a far-red fluorophore, Cyanine5 (Cy5), was conjugated with the RMN peptide probe to replace the FITC dye (table S3). Upon intravenous injection of Cy5-labeled RMN or MN probe, the blood was collected at designated time points for fluorescence measurements. As shown in Fig. 4E, both RMN and MN probes showed a nonlinear and time-dependent elimination curve over a period of 48 hours. However, the levels of RMN probe in the blood (~32.5%) remained higher than that in the MN group (~1.7%) at 48 hours postinjection. On the basis of the classical two-compartment model in pharmacokinetic studies, the elimination half-lives of RMN and MN peptide probes in the blood were determined as 38.5 ± 5.7 hours and 12.7 ± 0.2 hours, respectively (Fig. 4F). When compared to the MN-treated mice, the area under the curve and mean residence time exhibited a 10.9-fold and 1.7-fold increase in the RMN-treated group, revealing an improved pharmacokinetics of peptide probe after conjugation with ERY1 peptide for RBC hitchhiking in the blood (Fig. 4, G and H).

Diagnosis of human ovarian tumor using RMN probe in vivo

Next, we investigated the diagnostic efficiency of the RMN peptide probe in the human ovarian tumor-bearing mice. A far-red fluorophore (Cy5) and its specific quencher (QSY21) were selected as a FRET pair to conjugate with the RMN peptide probe through an amide condensation reaction. The photophysical properties of the Cy5/QSY21-modified RMN probe (Cy5/QC-RMN) and a control peptide probe without quencher modification (Cy5-RMN) were measured in PBS (fig. S6 and table S3). As shown in Fig. 5A, the absorbance peak of Cy5-RMN shifted from 650 to 660 nm in the absorbance of Cy5/QC-RMN, and the main emission peak of Cy5-RMN at 665 nm was markedly quenched upon QSY21 conjugation. The fluorescence emission at 665 nm of Cy5/QC-RMN was gradually elevated with the addition of MMP-2 or MMP-9, suggesting a concentration-dependent manner of enzyme-responsive Cy5/QC-RMN peptide probe (Fig. 5B and fig. S19). To develop a murine model of human ovarian cancer, the N-cadherin and MMPs overexpressed SKOV3 tumor cells were subcutaneously implanted into the right flank of BALB/c nude mice (Fig. 5C and fig. S20). When the tumor size reached 100 mm^3 (~day 30), the nude mice were intravenously injected with either free Cy5, Cy5-MN, Cy5-RMN, Cy5/QC-MN, or Cy5/QC-RMN at the same fluorophore dosage (50 μg/kg, $n = 3$), respectively. The PBS-treated mice were used as a control group. At predetermined time points after injection, the fluorescence signals in tumor tissues were measured on the basis of an In Vivo Imaging System (IVIS). As shown in Fig. 5D, the fluorescence signal gradually accumulated at the tumor site in the Cy5-RMN–treated mice rather than in the Cy5-MN or free Cy5 groups. We also analyzed the RBCs isolated from tumor tissues by flow cytometry based on the dye-labeled anti-mouse antibody of Ter119 (a classical erythroid surface marker). A 4.2-fold fluorescence increase of RMN-labeled $Ter119^+$-RBC was found in the tumor tissues of RMN-treated mice when compared to that in the MN-treated mice (fig. S21), suggesting an enhanced accumulation of RMN in the tumor region through RBC hitchhiking due to the prolonged circulation time. However, extensive fluorescence signal distribution was observed in the whole body of Cy5-RMN–treated mice, thus eliminating the accuracy of fluorescent probes for tumor diagnosis. Upon modification with a FRET pair, the fluorescence signal of Cy5/QC-RMN was only visualized in the tumor region of mice, suggesting an improved diagnosis efficiency of the RBC-hitchhiking RMN probe. When quantifying the MFI values in the tumor regions, the Cy5/QC-RMN–treated mice exhibited a maximum fluorescence signal at 1 hour postinjection, which underwent a marked fluorescence decrease when the tumor tissues were pretreated with the MMPs inhibitor GM6001 (Fig. 5E and fig. S22). To confirm these observations, tumor tissues were harvested from mice at 1 hour after administration of various peptide probes and further sectioned for ex vivo imaging. When normalized to the fluorescence signals of N-cadherin–targeting Cy5-MN–treated groups, the relative MFI values in the tumor tissue exhibited a significant augmentation in the mice treated with Cy5-RMN (1.42-fold increase), Cy5/QC-MN (1.14-fold increase), and Cy5/QC-RMN (2.85-fold increase), respectively (Fig. 5F and fig. S23). We also observed the strongest fluorescence signals of Cy5 in the frozen sections of tumor tissues upon Cy5/QC-RMN treatment compared to other control groups, indicating a rapid and effective diagnosis of primary ovarian tumor in vivo (Fig. 5, F and G).

We also performed the fluorescent screening of Cy5/QC-RMN in the major organs (e.g., heart, liver, spleen, lungs, and kidneys) to explore the potential metastasis, a major challenge in clinics that causes the death of patients with ovarian cancer after surgery. As shown in Fig. 4H, at 1 hour postinjection, the Cy5-MN was rapidly cleared from the main organs of mice, while the Cy5-RMN was widely distributed into various organs (especially the lung and kidneys) due to the prolonged circulation time (Figs. 4E and 5D). It is

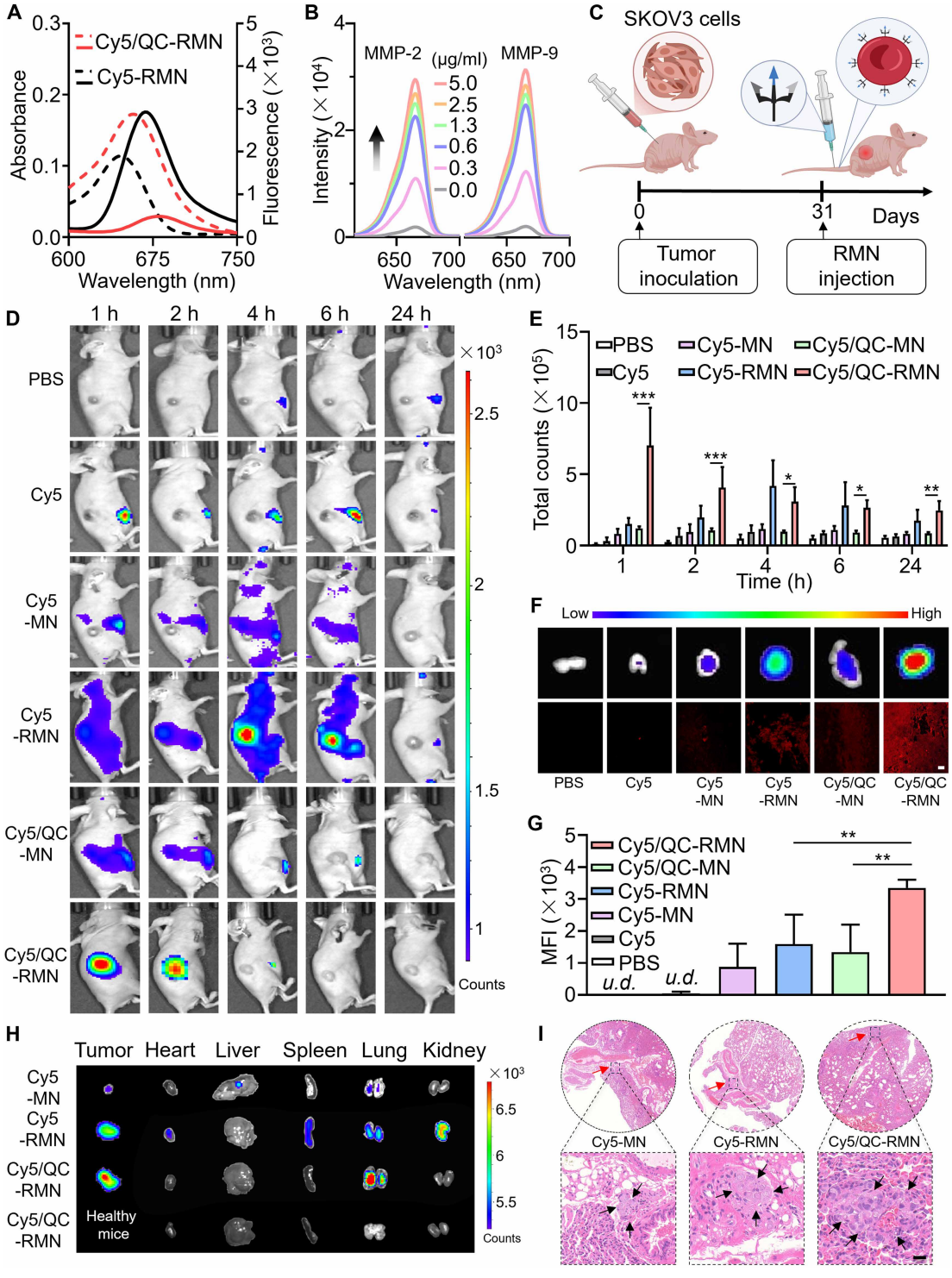

Fig. 5. Diagnosis of human ovarian tumor using RMN fluorescent probe in vivo. (**A**) Absorbance (dashed lines) and fluorescence emission spectra (solid lines) of Cy5/QC-RMN and Cy5-RMN in PBS. (**B**) Responsiveness of Cy5/QC-RMN probe (30 μg/ml) in the presence of activated MMP-2 and MMP-9 enzymes (5 μg/ml) for 30 min. (**C**) Schematic overview of the experimental timeline for the in vivo studies. Created in BioRender. Lin, Y. (2025) https://BioRender.com/n6w6wm6. (**D** and **E**) In vivo imaging (D) and total fluorescence counts (E) of SKOV3 tumor-bearing mice after intravenous injection of PBS, free Cy5, Cy5-MN, Cy5-RMN, Cy5/QC-MN, and Cy5/QC-RMN at different time points. h, hours. (**F**) Fluorescent images of isolated ovarian tumor tissues (top) and frozen sections (bottom) at 1 hour postinjection in different groups. Scale bar, 20 μm. (**G**) Quantitative analysis of MFI in the frozen sections of ovarian tumor tissues. u.d., undetected. (**H**) Fluorescence imaging of tumor tissues and major organs (heart, liver, spleen, lungs, and kidneys) at 1 hour postinjection of PBS, Cy5-RMN, and Cy5/QC-RMN in tumor-bearing and healthy mice. (**I**) Representative hematoxylin and eosin (H&E) images of lung tissue sections in different groups. Black arrows delineate the small metastatic foci in the lungs. Scale bar, 40 μm.

well-known that the kidneys are responsible for the rapid clearance of hydrophilic molecules injected into the blood. Thus, it was difficult to distinguish the tumor metastasis or natural metabolism in the lung and kidneys based on the enhanced fluorescence signals of Cy5-RMN in vivo. When the tumor-bearing mice were intravenously administered with Cy5/QC-RMN, we only found a strong fluorescence signal in the lung tissues besides the primary tumor region (Fig. 5H and fig. S24), and no obvious fluorescence signal was determined in the main organs of healthy mice, implying the possible metastatic foci in the lung. To confirm the tumor metastasis, the tissues of all major organs were sectioned for hematoxylin and eosin (H&E) staining. As shown in Fig. 5I and fig. S25, small metastatic foci were only determined in the lung, but not in other organs such as kidneys in all of the ovarian tumor-bearing mice. The lung metastases were further confirmed on the basis of the immunohistochemical staining of epithelial cell adhesion molecule, an overexpressed transmembrane glycoprotein in primary and metastatic ovarian cancer (fig. S26). Together, these results demonstrated that the Cy5/QC-RMN rather than other fluorescent molecules could serve as an effective fluorescent probe for the rapid and precise diagnosis of unknown human ovarian tumor metastasis in the living body.

Ex vivo diagnosis of human ovarian tumor tissues in clinics

Last, to further assess the feasibility of the Cy5/QC-RMN probe for the diagnosis of various human ovarian cancers in clinics, we collected several ovarian tumor tissues from different patients after surgery and confirmed their subtypes, including ovarian seromucinous borderline tumor (SMBT), HGSOC, and CCOC, based on the conventional immunohistochemical staining (fig. S27). Subsequently, different kinds of ovarian tumor tissues were incubated with the Cy5/QC-RMN for 30 min in PBS (Fig. 6A). Normal ovarian tissues were selected as the control group. After washing thrice with PBS, the fluorescence signals of them were measured by IVIS. As shown in Fig. 6 (B and C) and fig. S28, strong fluorescence signals were determined in all of these ovarian tumor tissues (SMBT, HGSOC, and CCOC) upon the treatment of Cy5/QC-RMN when compared to the normal ovarian tissues, although the expression levels of N-cadherin were obviously different in various subtypes of ovarian cancer. Moreover, histological examinations were further performed on the cross sections of SMBT tissues with lower N-cadherin expression than other subtypes of ovarian cancer. As shown in Fig. 6D and fig. S27, H&E staining results exhibited the obvious histopathological characterizations of SMBT in the ovarian tumor tissues, including the multinucleated tumor giant cells, eosinophilic nucleoli, and frequent mitotic figures (*9*). The confocal imaging of frozen sections further confirmed that the Cy5/QC-RMN probe had a higher red fluorescence signal in the SMBT tissues (392-fold increase) compared to the normal ovarian tissues in patients (Fig. 6E). Together, these results demonstrated that the Cy5/QC-RMN probe could effectively diagnose different kinds of human ovarian cancer in clinical samples.

Biosafety of RMN probe in vivo

Additionally, we assessed the biosafety of the RMN peptide probe in vivo. In this study, the highest injection dosage (300 μg/kg, $n = 3$) was injected into the tail vein of healthy mice. After 7 days postinjection, the hematological and blood biochemical evaluations were first performed in the mice. As shown in Fig. 6F, various hemocytes, including white blood cells (WBCs), lymphocytes (Lymph), monocytes (Mon), granulocytes (Gran), RBCs, and platelets (PLT), were comparable to those of the control mice treated with PBS. Meanwhile, the comprehensive blood chemistry parameters were consistent with those of the healthy mice, including the hepatic biomarkers such as alanine transaminase (ALT) and aspartate transferase (AST), as well as the renal biomarkers such as blood urea nitrogen (BUN), creatinine (CREA), and uric acid (UA) (Fig. 6G). To evaluate the potential adverse effects, major organs (e.g., heart, liver, spleen, lungs, and kidneys) were also harvested for histological analysis. As shown in Fig. 6H, no obvious pathological changes were observed in the H&E sections of all organs. Overall, these data suggested the excellent biosafety of RMN peptide as a diagnostic probe in living animals.

DISCUSSION

In summary, we demonstrated that the trident-like fluorescent peptide probe represents a promising approach to improve the intraoperative diagnosis efficiency of ovarian tumor with prolonged blood circulation time in vivo. In principle, this RBC-hitchhiking platform can be applied to conjugate various contrast agents or therapeutic drugs for enhanced pharmacokinetic profiles, thereby improving their diagnostic or therapeutic efficacy in diverse malignancies. Moreover, it can be adapted to additional conjugation strategies that specifically respond to the unique tumor microenvironment, including low pH and oxygen level, amplified inflammation and reactive oxygen species, and overexpressed enzymes (*67*). These strategies could further enhance the selectivity, sensitivity, and versatility of targeted delivery in vivo, ensuring a precise delivery of diagnostic or therapeutic agents to targeted tumor sites. Moreover, this biomimetic delivery strategy holds great promise to be applied to other circulatory blood cells, including neutrophils, monocytes or macrophages, and lymphocytes, to facilitate the blood cell–mediated delivery systems by leveraging their natural homing properties toward inflammatory tumor sites, thus fulfilling precise tumor diagnosis and therapy (*68*–*71*). Overall, the RBC-hitchhiking trident-like fluorescent probe offers extensive prospects for clinical translation in advancing the real-time visualization of ovarian tumors and metastatic lesions during FGS.

MATERIALS AND METHODS

Ovarian tumor tissues from patients

Human ovarian tumor tissues (60 cases) and normal ovarian tissues (14 cases) were obtained from patients treated at Ruijin Hospital (2018 to 2025), Shanghai Jiao Tong University School of Medicine, and further examined by pathologists (table S1 and S2). All experiments were approved by the ethics committees of research involving human subjects at Shanghai Jiao Tong University School of Medicine (nos. 2017-137, 2024-540, and 2025-157) and conducted with the understanding and informed consent of the patients in clinics. The research procedures conformed to the standards set by the Declaration of Helsinki. To evaluate the N-cadherin expression between human ovarian tumor and normal ovarian tissues, the resected ovaries from patients were fixed in 4% paraformaldehyde, and the tissue sections were stained by anti–N-cadherin antibody (Abcam, 1:1000) based on the standard protocols for immunohistochemistry analysis. The slides were scanned by a panoramic digital scanner (3DHISTECH,

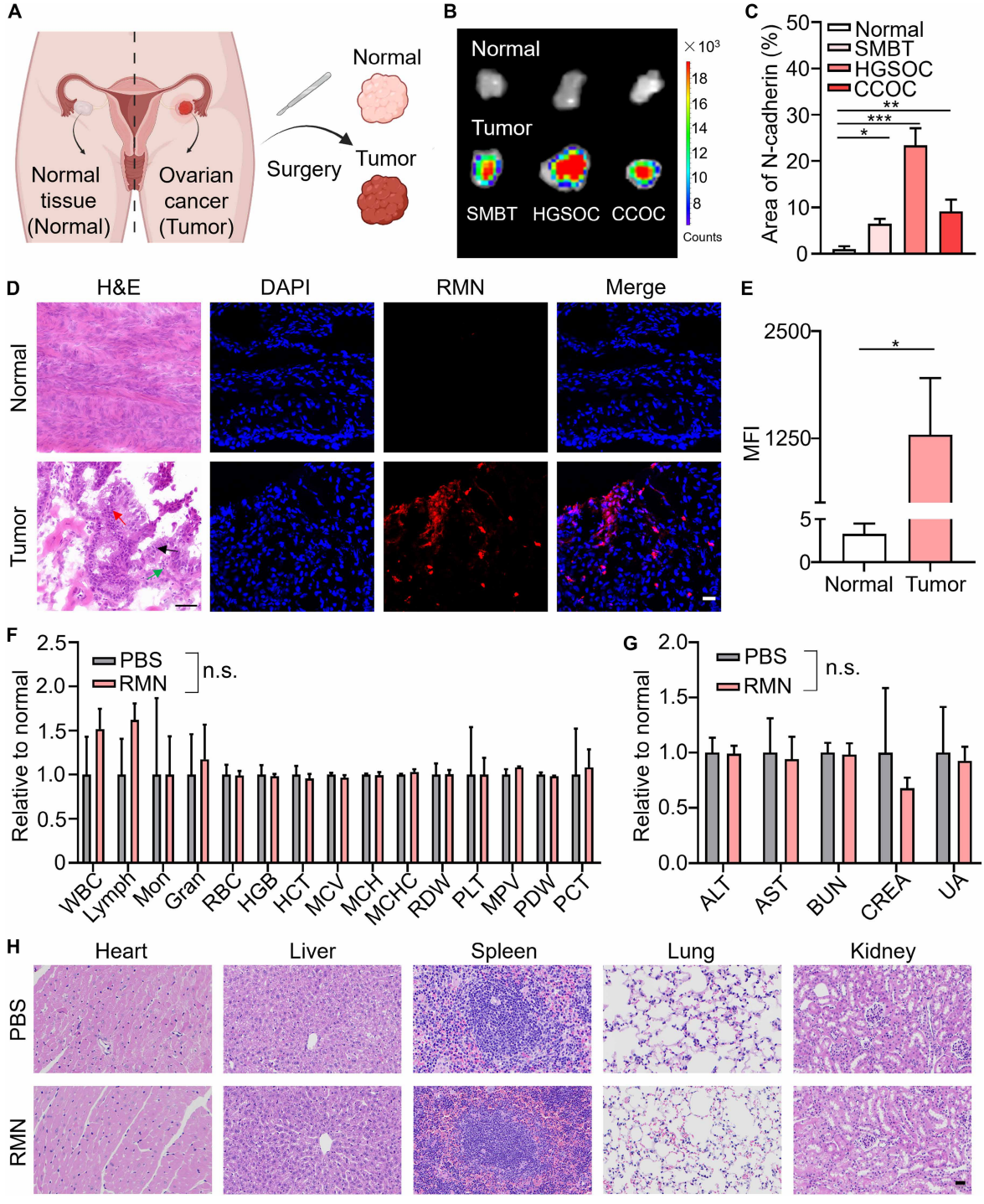

Fig. 6. Diagnosis of human ovarian tumor tissues from patients by RMN fluorescent probe and biosafety studies. (**A**) Schematic illustration of the experimental process for the ex vivo diagnosis of ovarian cancer in clinics. Human ovarian tumor tissues and normal ovarian tissues were collected from patients by surgery and incubated with Cy5/QC-RMN probe (30 μg/ml) for 30 min, followed by fluorescence imaging. Created in BioRender. Lin, Y. (2025) https://BioRender.com/n6w6wm6. (**B**) Representative fluorescent images of the normal and tumor ovarian tissues treated with the Cy5/QC-RMN probe. (**C**) Quantification of N-cadherin expression in ovarian tumor tissues (SMBT, HGSOC, and CCOC) and normal ovarian tissues using ImageJ software. (**D**) Representative H&E staining and frozen sections of human ovarian tumor tissues. Arrows mark multinucleated tumor giant cells (black), eosinophilic nucleoli (red), and frequent mitotic figures (green), respectively. Normal ovarian tissues were used as a control group. Scale bar, 40 μm. (**E**) Quantification of MFI in the frozen sections of ovarian tumor tissues in patients. (**F** to **H**) Amount of blood cells (F), comprehensive blood chemistry parameters (G), and H&E staining of main organs (heart, liver, spleen, lungs, and kidneys) (H) at day 7 after intravenous injection of PBS or Cy5/QC-RMN probe in healthy mice. Scale bar, 20 μm. n.s., not significant.

Hungary) and analyzed by Aipathwell software (Servicebio, China) to obtain the staining intensity and positive cell ratio. The positive grade of staining intensity was classified into 0 (negative without coloring), 1 (weak staining with light yellow), 2 (moderate staining with brownish yellow), and 3 (strong staining with sepia). The histochemical scoring (*H*-score, 0 to 300) was calculated {*H*-score = [(% of weak staining) × 1] + [(% of moderate staining) × 2] + [(% of strong staining) × 3]} to evaluate the overall percentage of N-cadherin positivity across the entire stained ovarian tumor tissues (*72*).

Databases

The freely accessible servers GTEx (www.gtexportal.org/) and TCGA (www.cancer.gov/tcga) were used to analyze the expression of N-cadherin in ovarian tumors ($n = 381$) and normal ovarian tissues ($n = 88$). The databases are chosen by including either primary or metastatic ovarian tumors, as well as filtering samples that do not have transcripts per million data. The gene expression data is extracted from both GTEx and TCGA datasets and further analyzed using various statistical methods and graphical representations. The demographic information was obtained from the TCGA database on the UALCAN website (https://ualcan.path.uab.edu).

Western blot assay in ovarian tumor cells

Human ovarian cancer cell lines (ES-2, OVCAR5, OVCAR8, A2780, HO-8910, OVCA433, and SKOV3), human breast cancer cells (MDA-MB-231 and BT-549), human liver cancer cells (HCCLM3 and HUH-7), mouse macrophages (RAW264.7), and HUVECs were purchased from the Cell Bank of the Chinese Academy of Sciences (Shanghai, China). ES-2 cells were cultured in a McCoy's 5A medium supplemented with 10% FBS and 1% penicillin-streptomycin (PS). OVCAR5, OVCAR8, HO-8910, OVCA433, SKOV3, and BT-549 cells were cultured in RPMI 1640 medium supplemented with 10% FBS and 1% PS. In addition, A2780, MDA-MB-231, HCCLM3, HUH-7, RAW264.7, and HUVECs were cultured in Dulbecco's modified Eagle's medium (DMEM) supplemented with 10% FBS and 1% PS. All cells were incubated at 37°C with 5% CO_2 in a humidity-controlled incubator. To evaluate the expression of N-cadherin in these cell lines, 5×10^6 cells were first lysed using a radioimmunoprecipitation assay buffer (Beyotime, China) containing phenylmethylsulfonyl fluoride (1 mM) as a serine protease inhibitor for 30 min on ice. Protein concentrations were quantified using a bicinchoninic acid protein assay kit (Thermo Fisher Scientific). Equal protein concentrations of all samples (2 mg/ml) were prepared in a certain proportion with 5× lithium dodecyl sulfate loading buffer, followed by heating at 100°C for 10 min. Then, 20 μl of samples were resolved by 10% SDS–polyacrylamide gel electrophoresis and run at 150 V for 1 hour. The separated proteins were transferred onto a polyvinylidene fluoride (PVDF) membrane (300 mA, 90 min), blocked in tris-buffered saline with 0.1% Tween 20 (TBST) buffer containing 5% skim milk, and then stained with primary anti–N-cadherin antibody (1:1000, Abcam) and anti–α-tubulin antibody (1:1000, Abcam) overnight at 4°C. Subsequently, PVDF membranes were rinsed with TBST five times and further incubated with horseradish peroxidase (HRP)–conjugated secondary antibodies against mouse immunoglobulin G (IgG) or rabbit IgG (1:3000, Biosharp) for 90 min at room temperature. After washing with TBST, the membranes were incubated with a chemiluminescent HRP substrate (Meilunbio, China) and visualized by a gel-imaging analysis system (Tanon-5200 Multi, China).

Molecular docking

The predicted structure of human N-cadherin was generated by AlphaFold and expanded to a three-dimensional model using Open Babel. AutoDock tools (ADT3) were used to prepare and parameterize the interaction between protein receptor (N-cadherin) and ligand (targeting peptide, LLGKCRAGVGRGC). The protonation state of all the compounds was set at pH 7.4 (25°C). The N-cadherin is represented as a slate cartoon model, the ligand is shown as a cyan stick, and their binding sites are shown as magenta stick structures. Nonpolar hydrogen atoms are omitted, and the hydrogen bonds (×Å) are depicted as yellow dashed lines. The equilibrium K_d (2.84×10^{-5} M) was calculated on the basis of the following formula

$$\Delta G = -RT\ln^{Kd}$$

where ΔG is the binding free energy (−6.2 kcal/mol calculated by molecular docking), R is the universal gas constant (8.314 J/K per mol), and T is temperature (298.15 K at 25°C).

Synthesis of ERY1-alkyne peptide

RBC hitchhiking peptide ERY1-alkyne [WMVLPWLPGTLDGGS GG(alkyne)RG-NH_2] was synthesized by Fmoc-chemistry–based SPPS using rink amide methylbenzhydrylamine (MBHA) resin (*73*). Briefly, the MBHA resin (0.2 mmol, 1 equiv, 0.664 mmol/g) was soaked in anhydrous dichloromethane (DCM) for 30 min and then treated with anhydrous dimethylformamide (DMF) containing 20% piperidine to deprotect the Fmoc group for 20 min. After washing thrice with DMF, a mixture of Fmoc-Gly-OH (1.5 equiv), *O*-benzotriazole-*N*,*N*,*N*′,*N*′-tetramethyl-uronium-hexafluorophosphate (HBTU; 1.5 equiv), 1-hydroxybenzotriazole (HOBT; 1.5 equiv), and diisopropylethylamine (DIPEA; 3 equiv) was incubated with the resins in DMF for stirring for 2 hours under a nitrogen (N_2) atmosphere. The resin was washed thrice with DMF to remove the unreacted reagents and further reacted with a mixture of acetic anhydride/DIPEA/DCM (v/v/v = 1:2:4) for 30 min to cap the unreacted amino groups. A repeated amide condensation reaction was performed with Fmoc-protected amino acids to synthesize the ERY1-alkyne peptide by replacing the Fmoc-Gly-OH with Fmoc-propargyl-Gly-OH. Last, the peptide was cleaved from the resins with a mixture of trifluoroacetic acid (TFA)/H_2O/triisopropylsilane (TPS) (v/v/v = 95:2.5:2.5) and stirred for 2 hours at room temperature. After removing the TFA under reduced pressure through an RV10 rotary evaporator (IKA, Germany), cold anhydrous ether was added into the flask to obtain ERY1-alkyne peptide as white precipitates. The peptide was lyophilized in a 10 mM HCl solution to remove residual TFA and directly applied for the next reaction without purification. Electrospray ionization mass spectrometry (ESI-MS; mass/charge ratio): calculated, 1993.32; found $[M]^+$, 1992.78.

Synthesis and characterization of RMN peptide probe

The synthesis of RBC-hitchhiking and ovarian cancer-targeting peptide probe (RMN) with a FRET pair (Quencher-K(ERY1)-GPAG↓LLG-K(dye)-CRAGVGRGC) was performed by Fmoc-chemistry–based SPPS using 2-chlorotrityl chloride resin (*74*). Briefly, the resin (0.2 mmol, 1 equiv, 0.565 mmol/g) was soaked in anhydrous DCM for 10 min and then reacted with Fmoc-Cys(Trt)-OH (1.5 equiv) and DIPEA (3 equiv) for 30 min. After being washed thrice with DCM, the unreacted groups on the resins were blocked with a mixture of methanol/DCM/DIPEA (v/v/v = 1:1:0.1) for 15 min. The Fmoc group on the

resin was deprotected by 20% piperidine in anhydrous DMF. Then, the resin was reacted with a mixture of Fmoc-Gly-OH (1.5 equiv), HBTU (1.5 equiv), HOBT (1.5 equiv), and DIPEA (3 equiv) in DMF for bubble stirring of 2 hours under an N_2 atmosphere and washed thrice with DMF to remove the unreacted reagents. A repeated amide condensation reaction was performed with Fmoc-protected amino acids to synthesize the ovarian cancer-targeting MN peptide by replacing the Fmoc-Lys(Boc)-OH with Fmoc-Lys(N_3)-OH. To conjugate the fluorescent dyes to the peptides, the Dde group of Fmoc-Lys(Dde)-OH on the resin was first cleaved to expose the NH_2 group by using hydroxylamine hydrochloride (125 mg, 1.8 mmol) and imidazole (92 mg, 1.35 mmol) in *N*-methylpyrrolidone (5 ml) with gentle magnetic stirring for 48 hours at room temperature. After washing thrice with DMF, the NH_2 group (1 equiv) was conjugated with 5/6-FITC (2 equiv) in DMF containing DIPEA (5 equiv) for bubble stirring overnight under an N_2 gas atmosphere or reacted with sulfo-Cy5 carboxylic acid (Cy5-COOH, 2 equiv) under catalyzing with HBTU/HOBT/DIPEA (both at 2 equiv) in DMF for 12 hours with magnetic stirring at room temperature in the dark. The quencher coupling on the resin was conducted by reacting a mixture of 4-(dimethylaminoazo)benzene-4-carboxylic acid (Dabcyl-COOH, 1.5 equiv), HBTU (2 equiv), HOBT (2 equiv), and DIPEA (2 equiv) for 12 hours or conjugating with QSY21 carboxylic acid succinimidyl ester (QSY21-NHS, 1.5 equiv) in DMF containing DIPEA (5 equiv) overnight in the dark. Last, click chemistry was performed between N_3-modified MN peptide (1 equiv) and ERY1-alkyne peptide (1.5 equiv) with the catalysis of copper(I) iodide (1.5 equiv) and DIPEA (90 equiv) in anhydrous DMF for 12 hours under an N_2 atmosphere. The resin was sequentially washed with saturated sodium ascorbate solution, 0.1 M EDTA in water, methanol, DMF, and DCM. Last, the peptide was cleaved from the resin with a mixture of TFA/H_2O/TPS (v/v/v = 95:2.5:2.5) and stirred for 2 hours at room temperature in the dark. After removing the TFA under reduced pressure, the peptide was precipitated with the addition of cold anhydrous ether and lyophilized in a 10 mM HCl solution. The peptide purification was performed using preparative HPLC (LC-2050, Shimadzu, Japan) with a reversed-phase C18 column (Agilent, Zorbax StableBond 300, 9.4 mm by 250 mm, 5 μm). The acetonitrile (0.1% of TFA) and water (0.1% of TFA) were used as the eluents with a flow rate of 10 ml/min. The process was monitored by ultraviolet (UV) absorbance at 220 and 280 nm. After removing the organic solvent under reduced pressure, the pure peptide was lyophilized in 10 mM HCl solution and characterized by HPLC, matrix-assisted laser desorption ionization–time of flight mass spectrometry, or ESI-MS (table S3). The absorbance and fluorescence spectra of various peptide probes were measured using a UV-Vis spectrophotometer (UV-2700, Shimadzu, Japan) and a fluorescence spectrophotometer (FL 6500, PerkinElmer, US). The stability of FITC-RMN and FITC/QC-RMN in PBS, 10% FBS, and 10% serum was measured at desired time points by a fluorescent microplate reader (excitation/emission, 488/525 nm).

Binding capability of RMN peptide probe in ovarian tumor cells

To evaluate the binding capability of the RMN peptide probe, FITC-RMN peptide [30 μg/ml; K(ERY1)-GPAG↓LLG-K(FITC)-CRAGVGRGC] was incubated with various human ovarian tumor cells (A2780, ES-2, OVCAR5, OVCA433, and SKOV3) or normal cells (HUVECs) for 30 min at 37°C in 96-well plates (1×10^4 cells per well). After washing thrice with 1× PBS, the fluorescence intensity was measured using a fluorescence microplate reader (excitation/emission, 488/525 nm). Then, the cells were fixed with 4% paraformaldehyde for 30 min, incubated with 4′,6-diamidino-2-phenylindole (DAPI) staining solution (Beyotime, China) for 10 min at room temperature, and fluorescence images were visualized using an upright fluorescence microscope (ECHO Revolve 4K Hybrid, US). Moreover, different concentrations of FITC-RMN peptide (0 to 30 μg/ml) were incubated with SKOV3 cells (3×10^5 cells) in RPMI 1640 medium for 30 min. The cells were washed with 1× PBS three times and analyzed with a CytoFLEX flow cytometer (Beckman, US). To visualize the peptide probe distribution in tumor cells, the SKOV3 cells were cultured in a confocal dish (3×10^5 cells per well) overnight and incubated with FITC-RMN peptide (30 μg/ml) for 30 min. Then, the cells were fixed with 4% paraformaldehyde, followed by the costaining with a DAPI and a far-red plasma membrane labeling kit (excitation/emission, 645/665 nm) for 30 min based on the manufacturer's instructions (Beyotime, China). After rinsing thrice with 1× PBS, the cell imaging was performed using a STELLARIS 5 confocal microscope (Leica, Germany). To visualize the internalization process of FITC-RMN in SKOV3 cells, the FITC-RMN was incubated with SKOV3 cells for 4 hours, and commercial lysosomal red tracker and nuclear-specific Hoechst 33342 were used to stain the lysosomes and nuclei in the cells, respectively. After rinsing thrice with 1× PBS, the cell imaging was analyzed using a STELLARIS 5 confocal microscope (Leica, Germany). To confirm the biocompatibility of RMN to ovarian tumor cells and normal cells, various concentrations of RMN (0, 1, 2, 4, 8, 16, and 32 μg/ml) were incubated with HUVEC, murine macrophages (RAW264.7), and human ovarian tumor cells (SKOV3), and their cell viability was estimated using the CCK-8 kit at 24 hours.

Enzyme responses of RMN peptide probe in vitro

The inactive proenzymes of MMPs (1 mM), such as pro–MMP-2 and pro–MMP-9, were first activated using 4-aminophenylmercuric acetate (1 mM) in the assay buffer (50 mM tris-HCl, 200 mM NaCl, 10 mM $CaCl_2$, 0.1 mM $ZnSO_4$, and 0.05% Brij-35, pH 7.4) for 1 hour at 37°C. Then, various peptide probes (30 μg/ml), including FITC/QC-RMN peptide [Dabcyl-K(ERY1)-GPAG↓LLG-K(FITC)-CRAGVGRGC] and Cy5/QC-RMN peptide [QSY21-K(ERY1)-GPAG↓LLG-K(Cy5)-CRAGVGRGC], were incubated with the activated MMPs (0, 0.2, 0.3, 0.6, 1.3, 2.5, and 5 μg/ml), other proteases (e.g., cathepsin B and trypsin, 5 μg/ml), and 50 μM MMPs inhibitor (GM6001) as controls in the assay buffer for 30 min. A microplate reader was used to determine the fluorescence intensity of FITC (excitation/emission, 488/525 nm) and Cy5 (excitation/emission, 645/665 nm), respectively. After centrifugation at 1000*g* for 30 min using Millipore Amicon Ultra Centrifugal Filters [30-kDa molecular weight cutoff (MWCO)] to remove the MMP enzymes, the cleaved peptides were analyzed by LC-MS (a Waters ACQUITY UPLC I-Class System equipped with a Vion IMS QTof MS, US). To determine the enzyme activities of MMPs in living cells, the various human ovarian cancer cells were cultured in six-well plates at a density of 1×10^6 cells per well for 24 hours. The medium was removed from cells and replaced with fresh culture media without FBS or with MMPs inhibitor (100 μM). After continuing incubation for 48 hours, the culture medium containing secreted MMPs was collected and concentrated by centrifugation at 1000*g* for 30 min using ultracentrifugal filters (MWCO, 30 kDa). The enzymes were further incubated with FITC/QC-RMN peptide (30 μg/ml) at 37°C for 30 min. The fluorescence intensity was measured by using a microplate reader (Tecan).

RBC-hitchhiking capability of RMN peptide probe

The whole blood of BALB/c nude mice was first collected via cardiac puncture using a syringe rinsed with heparin solution (100 U/ml) and transferred into blood collection tubes with EDTA anticoagulant. After centrifugation at 500*g* for 10 min at 4°C, the erythrocytes were collected in the pellet and suspended in the cold 1× PBS (pH 7.4). Then, FITC-RMN peptide (30 μg/ml) was incubated with 5% (v/v) mouse RBC at 37°C for 30 min, followed by washing twice with cold 1× PBS upon centrifuging (1000*g*, 5 min, 4°C). The fluorescence signal of FITC-RMN peptide on erythrocytes was determined using a microplate reader (excitation/emission, 488/525 nm) or visualized by an upright fluorescence microscope (ECHO Revolve 4K Hybrid, US) upon treatment with 4% paraformaldehyde for 30 min. The erythrocytes were also fixed with 2.5% glutaraldehyde and dehydrated with 30 to 100% gradient alcohol. After coating with a thin gold layer, SEM imaging was performed using an acceleration voltage of 2 KV (SU2080, Hitachi, Japan) and pseudocolored by Adobe Photoshop software. The unhitchhiking FITC-MN peptide [K(N_3)-GPAG↓LLG-K(FITC)-CRAGVGRGC] and PBS-treated RBCs were used as control groups. To evaluate the safety of peptide probes for erythrocytes, the standard agglutination and hemolysis assays were performed on the basis of the schedule described previously (*56*, *75*). Briefly, different concentrations of RMN peptide (0 to 30 μg/ml) were first incubated with 5% (v/v) mouse RBC (100 μl in 1× PBS) at 37°C for 30 min. Then, 50 μl of mixture was added into a round-bottom 96-well plate and incubated at 37°C for 1 hour. Agglutination is visually assessed as a pellet without a clear boundary. Mouse RBCs treated by PHA (0.1 mg/ml) were used as a positive control. To determine the degree of RBC hemolysis, various concentrations of RMN peptide (0 to 30 μg/ml) were first incubated with 5% (v/v) mouse RBC (100 μl in 1× PBS) at 37°C for 30 min, followed by centrifugation at 13,300*g* for 5 min. After that, the hemoglobin in the supernatant was quantified at an absorbance of 540 nm by a microplate reader. Mouse RBC with full hemolysis upon bath sonication was set as a positive control, and the RBC treated by PBS only was used as a negative control. The equilibrium K_d between the RBC-hitchhiking peptide (ERY1) and the glycophorin A protein was calculated using a molecular docking model. To verify the stability of RMN on the RBC surface, FITC-RMN was incubated with whole blood and collected RBCs at different time points (0, 1, 3, 6, 12, and 24 hours) to analyze fluorescence signals.

Pharmacokinetic studies of RMN probe in vivo

All of the animal experiments were approved and guided by the Institutional Animal Care and Use Committee of Shanghai Jiao Tong University (no. A2024191). For the blood circulation study, 100 μl of Cy5-RMN peptide probes (0.15 mg/kg, $n = 3$) were intravenously injected into the BALB/c nude mice (6 to 8 weeks, female). The unhitchhiking Cy5-MN [K(N_3)-GPAG↓LLG-K(Cy5)-CRAGVGRGC] and PBS-treated mice were used as control groups. A drop of blood (~30 μl) was collected from each mouse via submandibular puncture with heparin-coated tubes at 0, 1, 2, 4, 8, 16, 24, and 48 hours postinjection. The collected blood (20 μl) was then diluted with 1× PBS (180 μl) under sonication. The fluorescence intensity of Cy5-RMN peptide in the blood was measured using a fluorescence microplate reader (excitation/emission, 645/665 nm). For the biodistribution study, human ovarian tumor-bearing BALB/c nude mice were intravenously administered with 100 μl of Cy5/QC-RMN peptide (50 μg/kg, $n = 3$). At 1 hour postinjection, the nude mice and their major organs (e.g., heart, liver, spleen, lungs, and kidneys) were imaged on the basis of the IVIS (PerkinElmer, US) to record the MFI.

Diagnosis of human ovarian tumor by RMN peptide probe in vivo

To develop a human ovarian tumor model, 5×10^6 SKOV3 cells were implanted subcutaneously into the right flank of BALB/c nude mice (6-week-old, female). Body weights and tumor volumes of mice were measured every 2 days, and tumor volumes were calculated using the equation: volume = (length × width^2)/2. When the average tumor size reached 100 mm^3 (~day 30), the tumor-bearing nude mice were intravenously injected with PBS, free Cy5, Cy5-MN, Cy5-RMN, Cy5/QC-MN, and Cy5/QC-RMN at the same Cy5 dosage (50 μg/kg, $n = 3$). The mice treated with PBS and MMPs inhibitor were used as control groups. At 1, 2, 4, 6, and 24 hours postinjection, the nude mice and their major organs (e.g., heart, liver, spleen, lungs, and kidneys) were imaged on the basis of the IVIS (PerkinElmer, US). The tumor tissues were collected and processed with frozen sections (3 to 5 μm) and H&E staining. The tumor tissues were imaged using a STELLARIS 5 confocal microscope (Leica, Germany), and the MFI was analyzed by ImageJ software. To evaluate the diagnostic capability of the peptide probe for human ovarian tumors in clinics, the freshly resected ovarian tumor tissues and normal ovarian tissues from patients (three cases) were coincubated with Cy5/QC-RMN peptide for 30 min at 37°C. After washing three times with 1× PBS, the ovarian tissues were imaged using an IVIS system (excitation/emission, 645/665 nm). The frozen sections of ovarian tissues were further stained with DAPI for 30 min, and fluorescence images were recorded using a STELLARIS 5 confocal microscope (Leica, Germany). The human ovarian tissues were further fixed in 4% paraformaldehyde overnight, followed by incubation with an increasing ethanol gradient (30 to 100%) and xylene in sequence. Then, the samples were embedded in paraffin and sectioned into 3- to 5-μm slides for H&E staining and immunohistochemistry staining. To investigate the RMN-RBC complexes in the tumor tissue, FITC-labeled RMN or MN probe was intravenously injected for 4 hours. The ovarian tumor tissues were collected and prepared for the single-cell suspension. In brief, tumor tissues were cut into small pieces and then digested in DMEM containing collagenase IV (1 mg/ml) and deoxyribonuclease I (200 units/ml) at 37°C for 30 min, followed by the resultant suspension being filtered through a 70-μm Falcon cell strainer and centrifuged at 300*g* for 5 min. Live cells were labeled by allophycocyanin-labeled anti-mouse Ter119 antibody and quantified by flow cytometry.

Biosafety studies of RMN peptide probe in vivo

To evaluate the biosafety of the peptide probe, healthy BALB/c nude mice (6 to 8 weeks, female) were intravenously injected with PBS or Cy5/QC-RMN peptide (300 μg/kg, $n = 3$). On day 7 postinjection, whole blood (500 μl) was collected through cardiac puncture and allowed to coagulate in an Eppendorf tube. After centrifugation at 2000*g* for 15 min, the serum was harvested for comprehensive blood chemistry analysis, including alanine transaminase (ALT), aspartate transferase (AST), blood urea nitrogen (BUN), creatinine (CREA), and uric acid (UA). In addition, 300 μl of whole blood was placed into an EDTA-coated anticoagulant tube for the complete blood counts, including WBC, lymphocyte (Lymph), monocytes (Mon), granulocytes (Gran), RBC, hemoglobin (HGB), hematocrit (HCT),

mean corpuscular volume (MCV), mean corpuscular hemoglobin (MCH), mean corpuscular hemoglobin concentration (MCHC), red cell distribution width (RDW), platelet (PLT), mean platelet volume (MPV), platelet distribution width (PDW), and plateletcrit (PCT). For histopathological examination, mice were euthanized, and their major organs (e.g., heart, liver, spleen, lungs, and kidneys) were resected, fixed in 4% paraformaldehyde for 24 hours, and sectioned for H&E staining.

Statistical analyses

All data in the studies were calculated and presented as means ± SD from at least three independent experiments. GraphPad Prism 8.0 software was applied for all graph generation and statistical analysis. Statistical significance was determined by the Student's two-tailed *t* test (*P* value: $*P < 0.1$, $**P < 0.01$, and $***P < 0.001$).

Supplementary Materials

This PDF file includes:

Figs. S1 to S28
Tables S1 to S3

REFERENCES AND NOTES

1. F. Bray, M. Laversanne, H. Sung, J. Ferlay, R. L. Siegel, I. Soerjomataram, A. Jemal, Global cancer statistics 2022: GLOBOCAN estimates of incidence and mortality worldwide for 36 cancers in 185 countries. *CA Cancer J. Clin.* **74**, 229–263 (2024).
2. S. Lheureux, M. Braunstein, A. M. Oza, Epithelial ovarian cancer: Evolution of management in the era of precision medicine. *CA Cancer J. Clin.* **69**, 280–304 (2019).
3. P. A. Konstantinopoulos, U. A. Matulonis, Clinical and translational advances in ovarian cancer therapy. *Nat. Cancer* **4**, 1239–1257 (2023).
4. N. Colombo, D. Lorusso, P. Scollo, Impact of recurrence of ovarian cancer on quality of life and outlook for the future. *Int. J. Gynecol. Cancer* **27**, 1134–1140 (2017).
5. D. D. Bowtell, S. Bohm, A. A. Ahmed, P. J. Aspuria, R. C. Bast Jr., V. Beral, J. S. Berek, M. J. Birrer, S. Blagden, M. A. Bookman, J. D. Brenton, K. B. Chiappinelli, F. C. Martins, G. Coukos, R. Drapkin, R. Edmondson, C. Fotopoulou, H. Gabra, J. Galon, C. Gourley, V. Heong, D. G. Huntsman, M. Iwanicki, B. Y. Karlan, A. Kaye, E. Lengyel, D. A. Levine, K. H. Lu, I. A. McNeish, U. Menon, S. A. Narod, B. H. Nelson, K. P. Nephew, P. Pharoah, D. J. Powell Jr., P. Ramos, I. L. Romero, C. L. Scott, A. K. Sood, E. A. Stronach, F. R. Balkwill, Rethinking ovarian cancer II: reducing mortality from high-grade serous ovarian cancer. *Nat. Rev. Cancer* **15**, 668–679 (2015).
6. Y. Li, Y. Cen, Y. Fang, S. Tang, S. Li, Y. Ren, H. Zhang, W. Lu, J. Xu, Breaking the iron homeostasis: A "Trojan horse" self-assembled nanodrug sensitizes homologous recombination proficient ovarian cancer cells to PARP inhibition. *ACS Nano* **16**, 12786–12800 (2022).
7. D. K. Armstrong, R. D. Alvarez, F. J. Backes, J. N. Bakkum-Gamez, L. Barroilhet, K. Behbakht, A. Berchuck, L. M. Chen, V. C. Chitiyo, M. Cristea, M. DeRosa, E. L. Eisenhauer, D. M. Gershenson, H. J. Gray, R. Grisham, A. Hakam, A. Jain, A. Karam, G. E. Konecny, C. A. Leath III, G. Leiserowitz, J. Liu, L. Martin, D. Matei, M. McHale, K. McLean, D. S. Miller, S. Percac-Lima, S. W. Remmenga, J. Schorge, D. Stewart, P. H. Thaker, R. Vargas, A. W. Hendrickson, T. L. Werner, E. Zsiros, M. A. Dwyer, L. Hang, NCCN Guidelines insights: Ovarian cancer, version 3.2022. *J. Natl. Compr. Canc. Netw.* **20**, 972–980 (2022).
8. Y. Xi, L. Sun, X. Che, X. Huang, H. Liu, Q. Wang, H. Meng, Y. Miao, Q. Qu, W. Hai, B. Li, W. Feng, A comparative study of [^{68}Ga]Ga-FAPI-04 PET/MR and [^{18}F]FDG PET/CT in the diagnostic accuracy and resectability prediction of ovarian cancer. *Eur. J. Nucl. Med. Mol. Imaging* **50**, 2885–2898 (2023).
9. M. A. Lisio, L. Fu, A. Goyeneche, Z. H. Gao, C. Telleria, High-grade serous ovarian cancer: Basic sciences, clinical and therapeutic standpoints. *Int. J. Mol. Sci.* **20**, 952 (2019).
10. S. K. Sharma, B. Nemieboka, E. Sala, J. S. Lewis, B. M. Zeglis, Molecular imaging of ovarian cancer. *J. Nucl. Med.* **57**, 827–833 (2016).
11. B. Zhang, J. Lu, X. Lin, J. Wang, Q. Li, T. Jin, Q. Shi, Y. Lu, J. Zhang, J. Deng, Y. Zhang, Y. Guo, J. Gao, H. Chen, Y. Yan, J. Wu, J. Gao, J. Che, X. Dong, Z. Gu, N. Lin, Injectable and sprayable fluorescent nanoprobe for rapid real-time detection of human colorectal tumors. *Adv. Mater.* **36**, e2405275 (2024).
12. J. Dai, Y. Cheng, J. Wu, Q. Wang, W. Wang, J. Yang, Z. Zhao, X. Lou, F. Xia, S. Wang, B. Z. Tang, Modular peptide probe for pre/intra/postoperative therapeutic to reduce recurrence in ovarian cancer. *ACS Nano* **14**, 14698–14714 (2020).
13. Q. T. Nguyen, R. Y. Tsien, Fluorescence-guided surgery with live molecular navigation — A new cutting edge. *Nat. Rev. Cancer* **13**, 653–662 (2013).
14. H. Singh, S. Rote, A. Jada, E. D. Bander, G. J. Almodovar-Mercado, W. I. Essayed, R. Hartl, V. K. Anand, T. H. Schwartz, J. P. Greenfield, Endoscopic endonasal odontoid resection with real-time intraoperative image-guided computed tomography: report of 4 cases. *J. Neurosurg.* **128**, 1486–1491 (2018).
15. T. Hussain, Q. T. Nguyen, Molecular imaging for cancer diagnosis and surgery. *Adv. Drug Deliv. Rev.* **66**, 90–100 (2014).
16. A. Mochida, F. Ogata, T. Nagaya, P. L. Choyke, H. Kobayashi, Activatable fluorescent probes in fluorescence-guided surgery: Practical considerations. *Bioorg. Med. Chem.* **26**, 925–930 (2018).
17. X. Liu, Y. T. Chang, Fluorescent probe strategy for live cell distinction. *Chem. Soc. Rev.* **51**, 1573–1591 (2022).
18. J. Mu, F. Liu, M. S. Rajab, M. Shi, S. Li, C. Goh, L. Lu, Q. H. Xu, B. Liu, L. G. Ng, B. Xing, A small-molecule FRET reporter for the real-time visualization of cell-surface proteolytic enzyme functions. *Angew. Chem. Int. Ed. Engl.* **53**, 14357–14362 (2014).
19. U. Tamima, S. Sarkar, M. R. Islam, A. Shil, K. H. Kim, Y. J. Reo, Y. W. Jun, H. Banna, S. Lee, K. H. Ahn, A small-molecule fluorescence probe for nuclear ATP. *Angew. Chem. Int. Ed. Engl.* **62**, e202300580 (2023).
20. R. Tian, H. Ma, S. Zhu, J. Lau, R. Ma, Y. Liu, L. Lin, S. Chandra, S. Wang, X. Zhu, H. Deng, G. Niu, M. Zhang, A. L. Antaris, K. S. Hettie, B. Yang, Y. Liang, X. Chen, A. Expand, Multiplexed NIR-II probes for lymph node-invaded cancer detection and imaging-guided surgery. *Adv. Mater.* **32**, e1907365 (2020).
21. Z. Hu, C. Fang, B. Li, Z. Zhang, C. Cao, M. Cai, S. Su, X. Sun, X. Shi, C. Li, T. Zhou, Y. Zhang, C. Chi, P. He, X. Xia, Y. Chen, S. S. Gambhir, Z. Cheng, J. Tian, First-in-human liver-tumour surgery guided by multispectral fluorescence imaging in the visible and near-infrared-I/II windows. *Nat. Biomed. Eng.* **4**, 259–271 (2020).
22. Y. Jiang, K. Pu, Molecular probes for autofluorescence-free optical imaging. *Chem. Rev.* **121**, 13086–13131 (2021).
23. Y. Feng, J. Fang, Y. Zhao, S. Ye, A. Wang, Y. Zhang, J. Zhu, J. Li, Z. Lv, Z. Zhao, H. Shi, NIR light-mediated mitochondrial RNA modification for cancer RNA interference therapeutics. *Angew. Chem. Int. Ed. Engl.* **62**, e202218969 (2023).
24. W. Zeng, D. Ye, Seeing cancer via sonoafterglow. *Nat. Biomed. Eng.* **7**, 197–198 (2023).
25. X. Yang, H. Lu, N. Kong, H. Wang, Confinement of assemblies of peptides by chemical reactions in living cells. *Chemistry* **29**, e202203145 (2023).
26. Q. Jia, R. Zhang, H. Yan, Y. Feng, F. Sun, Z. Yang, C. Qiao, X. Mou, J. Tian, Z. Wang, An activatable near-infrared fluorescent probe for precise detection of the pulmonary metastatic tumors: A traditional molecule having a stunning turn. *Angew. Chem. Int. Ed. Engl.* **62**, e202313420 (2023).
27. Y. Zhang, D. Liu, W. Chen, Y. Tao, W. Li, J. Qi, Microenvironment-activatable probe for precise NIR-II monitoring and synergistic immunotherapy in rheumatoid arthritis. *Adv. Mater.* **36**, e2409661 (2024).
28. J. S. D. Mieog, F. B. Achterberg, A. Zlitni, M. Hutteman, J. Burggraaf, R. J. Swijnenburg, S. Gioux, A. L. Vahrmeijer, Fundamentals and developments in fluorescence-guided cancer surgery. *Nat. Rev. Clin. Oncol.* **19**, 9–22 (2022).
29. C. Ren, J. Zhang, M. Chen, Z. Yang, Self-assembling small molecules for the detection of important analytes. *Chem. Soc. Rev.* **43**, 7257–7266 (2014).
30. D. Xu, L. Li, C. Chu, X. Zhang, G. Liu, Advances and perspectives in near-infrared fluorescent organic probes for surgical oncology. *Wiley Interdiscip. Rev. Nanomed. Nanobiotechnol.* **12**, e1635 (2020).
31. M. Z. Cai, Z. Wen, H. Z. Li, Y. Yang, J. X. Liang, Y. S. Liao, J. Y. Wang, L. Y. Wang, N. Y. Zhang, K. I. Kamei, H. W. An, H. Wang, Peptide-based fluorescent probes for the diagnosis of tumor and image-guided surgery. *Biosens. Bioelectron.* **276**, 117255 (2025).
32. L. Yu, Y. Peng, L. Jiang, L. Qiu, Sequential diagnosis and treatment for colon cancer via derived iridium and indocyanine green hybrid nanomicelles. *ACS Appl. Mater. Interfaces* **15**, 34617–34630 (2023).
33. W. Chen, Y. Zhang, L. Zhang, X. Luo, X. Yang, Y. Zhu, G. Wang, W. Huang, D. Zhang, Y. Zeng, R. Li, C. Guo, J. Wang, Z. Wu, N. Liu, G. Zhang, Intraoperative evaluation of tumor margins using a TROP2 near-infrared imaging probe to enable human breast-conserving surgery. *Sci. Transl. Med.* **16**, eado2461 (2024).
34. Y. Chen, W. Liu, B. Li, X. Gao, K. Zhou, M. Zhang, G. Yang, M. Cui, Synthesis, preclinical evaluation, and first-in-human assessment of ICG-PSMA-D5: A PSMA-targeted probe for fluorescence-guided surgery of prostate cancer. *J. Med. Chem.* **68**, 3858–3872 (2025).
35. Y. Gao, C. Berciu, Y. Kuang, J. Shi, D. Nicastro, B. Xu, Probing nanoscale self-assembly of nonfluorescent small molecules inside live mammalian cells. *ACS Nano* **7**, 9055–9063 (2013).
36. X. Shi, Y. Deng, X. Liu, G. Gao, R. Wang, G. Liang, An aminopeptidase N-activatable chemiluminescence probe for image-guided surgery and metastasis tracking of tumor. *Biosens. Bioelectron.* **208**, 114212 (2022).
37. A. Razgulin, N. Ma, J. Rao, Strategies for in vivo imaging of enzyme activity: An overview and recent advances. *Chem. Soc. Rev.* **40**, 4186–4216 (2011).
38. X. Zhen, X. Jiang, Polymer-based activatable optical probes for tumor fluorescence and photoacoustic imaging. *Wiley Interdiscip. Rev. Nanomed. Nanobiotechnol.* **12**, e1593 (2020).

39. H. Lee, J. Kim, H. Kim, Y. Kim, Y. Choi, A folate receptor-specific activatable probe for near-infrared fluorescence imaging of ovarian cancer. *Chem. Commun.* **50**, 7507–7510 (2014).
40. B. Shi, Z. Zhang, Q. Jin, Z. Wang, J. Tang, G. Xu, T. Zhu, X. Gong, X. Tang, C. Zhao, Selective tracking of ovarian-cancer-specific gamma-glutamyltranspeptidase using a ratiometric two-photon fluorescent probe. *J. Mater. Chem. B* **6**, 7439–7443 (2018).
41. H. Kobayashi, P. L. Choyke, Target-cancer-cell-specific activatable fluorescence imaging probes: Rational design and in vivo applications. *Acc. Chem. Res.* **44**, 83–90 (2011).
42. H. Kobayashi, M. R. Longmire, M. Ogawa, P. L. Choyke, Rational chemical design of the next generation of molecular imaging probes based on physics and biology: Mixing modalities, colors and signals. *Chem. Soc. Rev.* **40**, 4626–4648 (2011).
43. D. Seah, Z. Cheng, M. Vendrell, Fluorescent probes for imaging in humans: Where are we now? *ACS Nano* **17**, 19478–19490 (2023).
44. Y. Ding, B. Lv, J. Zheng, C. Lu, J. Liu, Y. Lei, M. Yang, Y. Wang, Z. Li, Y. Yang, W. Gong, J. Han, C. Gao, RBC-hitchhiking chitosan nanoparticles loading methylprednisolone for lung-targeting delivery. *J. Control. Release* **341**, 702–715 (2022).
45. B. Yu, Y. Liu, Y. Zhang, L. Xu, K. Jin, A. Sun, X. Zhao, Y. Wang, H. Liu, An SS31-rapamycin conjugate via RBC hitchhiking for reversing acute kidney injury. *Biomaterials* **303**, 122383 (2023).
46. M. Shen, H. Jiang, Y. Zhao, L. Wu, H. Yang, Y. Yao, H. Meng, Q. Yang, L. Liu, Y. Li, Shear stress and ROS dual-responsive RBC-hitchhiking nanoparticles for atherosclerosis therapy. *ACS Appl. Mater. Interfaces* **15**, 43374–43386 (2023).
47. J. S. Brenner, S. Mitragotri, V. R. Muzykantov, Red blood cell hitchhiking: A novel approach for vascular delivery of nanocarriers. *Annu. Rev. Biomed. Eng.* **23**, 225–248 (2021).
48. J. W. Lee, H. Y. Yoon, Y. J. Ko, E. H. Kim, S. Song, S. Hue, N. Gupta, D. Malin, J. Kim, B. Kong, S. Kim, I. S. Kim, I. C. Kwon, Y. Yang, S. H. Kim, Dual-action protein-siRNA conjugates for targeted disruption of CD47-signal regulatory protein α axis in cancer therapy. *ACS Nano* **18**, 22298–22315 (2024).
49. J. Li, Y. Ding, Q. Cheng, C. Gao, J. Wei, Z. Wang, Q. Huang, R. Wang, Supramolecular erythrocytes-hitchhiking drug delivery system for specific therapy of acute pneumonia. *J. Control. Release* **350**, 777–786 (2022).
50. P. H. D. Nguyen, M. K. Jayasinghe, A. H. Le, B. Peng, M. T. N. Le, Advances in drug delivery systems based on red blood cells and their membrane-derived nanoparticles. *ACS Nano* **17**, 5187–5210 (2023).
51. T. M. H. Huynh, B. N. Yalamandala, M. R. Chiang, W. H. Weng, C. W. Chang, W. H. Chiang, L. D. Liao, Y. C. Liu, S. H. Hu, Programmed antigen capture-harnessed dendritic cells by margination-hitchhiking lung delivery. *J. Control. Release* **358**, 718–728 (2023).
52. P. M. Glassman, E. D. Hood, L. T. Ferguson, Z. Zhao, D. L. Siegel, S. Mitragotri, J. S. Brenner, V. R. Muzykantov, Red blood cells: The metamorphosis of a neglected carrier into the natural mothership for artificial nanocarriers. *Adv. Drug Deliv. Rev.* **178**, 113992 (2021).
53. H. Yang, J. N. Zhou, X. M. Zhang, D. D. Ling, Y. B. Sun, C. Y. Li, Q. Q. Zhou, G. N. Shi, S. H. Wang, X. S. Lin, T. Fan, H. Y. Wang, Q. Zeng, Y. L. Jia, J. F. Xi, Y. G. Jin, X. T. Pei, W. Yue, Nanoengineered red blood cells loaded with TMPRSS2 and cathepsin L inhibitors block SARS-CoV-2 pseudovirus entry into lung ACE2^{+} cells. *Adv. Mater.* **36**, e2310306 (2024).
54. M. Wu, Z. Luo, Z. Cai, Q. Mao, Z. Li, H. Li, C. Zhang, Y. Zhang, A. Zhong, L. Wu, X. Liu, Spleen-targeted neoantigen DNA vaccine for personalized immunotherapy of hepatocellular carcinoma. *EMBO Mol. Med.* **15**, e16836 (2023).
55. H. Yu, Y. Piao, Y. Zhang, J. Xiang, S. Shao, J. Tang, Z. Zhou, Y. Shen, Cell-selective binding zwitterionic polymeric micelles boost the delivery efficiency of antibiotics. *ACS Nano* **17**, 22430–22443 (2023).
56. L. T. Ferguson, E. D. Hood, T. Shuvaeva, V. V. Shuvaev, M. C. Basil, Z. Wang, J. Nong, X. Ma, J. Wu, J. W. Myerson, O. A. Marcos-Contreras, J. Katzen, J. M. Carl, E. E. Morrisey, E. Cantu, C. H. Villa, S. Mitragotri, V. R. Muzykantov, J. S. Brenner, Dual affinity to RBCs and target cells (DART) enhances both organ- and cell type-targeting of intravascular nanocarriers. *ACS Nano* **16**, 4666–4683 (2022).
57. T. C. Binns, D. A. Eaton, D. V. Akiki, E. Deschenes, A. S. Piotrowski-Daspit, L. G. Bracaglia, J. E. Hendrickson, W. M. Saltzman, Cellular determinants influence the red blood cell adsorption efficiency of poly(amine-co-ester) nanoparticles. *Sci. Adv.* **11**, eadt8637 (2025).
58. H. Yao, Z. Wang, N. Wang, Z. Deng, G. Liu, J. Zhou, S. Chen, J. Shi, G. Zhu, Enhancing circulation and tumor accumulation of carboplatin via an erythrocyte-anchored prodrug strategy. *Angew. Chem. Int. Ed. Engl.* **61**, e202203838 (2022).
59. Z. Zhao, A. Ukidve, V. Krishnan, A. Fehnel, D. C. Pan, Y. Gao, J. Kim, M. A. Evans, A. Mandal, J. Guo, V. R. Muzykantov, S. Mitragotri, Systemic tumour suppression via the preferential accumulation of erythrocyte-anchored chemokine-encapsulating nanoparticles in lung metastases. *Nat. Biomed. Eng.* **5**, 441–454 (2021).
60. A. R. Loftis, G. Zhang, C. Backlund, A. J. Quartararo, N. Pishesha, C. C. Hanna, C. K. Schissel, D. Garafola, A. Loas, R. J. Collier, H. Ploegh, D. J. Irvine, B. L. Pentelute, An in vivo selection-derived d-peptide for engineering erythrocyte-binding antigens that promote immune tolerance. *Proc. Natl. Acad. Sci. U.S.A.* **118**, e2101596118 (2021).
61. C. Sun, R. K. Jain, L. L. Munn, Non-uniform plasma leakage affects local hematocrit and blood flow: Implications for inflammation and tumor perfusion. *Ann. Biomed. Eng.* **35**, 2121–2129 (2007).
62. K. Chen, X. Yuan, S. Wang, F. Zheng, Z. Fu, Z. Shen, X. Cheng, Y. Wang, S. Tang, H. Ni, F. Wang, G. Lu, Y. Wu, D. Xia, W. Lu, MAP4K4 promotes ovarian cancer metastasis through diminishing ADAM10-dependent N-cadherin cleavage. *Oncogene* **42**, 1438–1452 (2023).
63. H. Ding, J. Zhang, F. Zhang, Y. Xu, W. Liang, Y. Yu, Nanotechnological approaches for diagnosis and treatment of ovarian cancer: A review of recent trends. *Drug Deliv.* **29**, 3218–3232 (2022).
64. S. Subramanian, A. C. Daquinag, S. AghaAmiri, S. C. Ghosh, A. Azhdarinia, M. G. Kolonin, Characterization of peptides targeting metastatic tumor cells as probes for cancer detection and vehicles for therapy delivery. *Cancer Res.* **81**, 5756–5764 (2021).
65. A. A. Kamat, M. Fletcher, L. M. Gruman, P. Mueller, A. Lopez, C. N. Landen Jr., L. Han, D. M. Gershenson, A. K. Sood, Editor's note: The clinical relevance of stromal matrix metalloproteinase expression in ovarian cancer. *Clin. Cancer Res.* **27**, 4455 (2021).
66. J. R. Tauro, B. S. Lee, S. S. Lateef, R. A. Gemeinhart, Matrix metalloprotease selective peptide substrates cleavage within hydrogel matrices for cancer chemotherapy activation. *Peptides* **29**, 1965–1973 (2008).
67. E. Denisenko, L. de Kock, A. Tan, A. B. Beasley, M. Beilin, M. E. Jones, R. Hou, D. O. Muiri, S. Bilic, G. Mohan, S. Salfinger, S. Fox, K. P. W. Hmon, Y. Yeow, Y. Kim, R. John, T. S. Gilderman, E. Killingbeck, E. S. Gray, P. A. Cohen, Y. Yu, A. R. R. Forrest, Spatial transcriptomics reveals discrete tumour microenvironments and autocrine loops within ovarian cancer subclones. *Nat. Commun.* **15**, 2860 (2024).
68. Z. Luo, Y. Lu, Y. Shi, M. Jiang, X. Shan, X. Li, J. Zhang, B. Qin, X. Liu, X. Guo, J. Huang, Y. Liu, S. Wang, Q. Li, L. Luo, J. You, Neutrophil hitchhiking for drug delivery to the bone marrow. *Nat. Nanotechnol.* **18**, 647–656 (2023).
69. K. Wei, Y. Xu, C. Nie, Q. Wei, P. Xie, T. Chen, J. Jiang, X. Chu, A multifunctional peptide nucleic acid/peptide copolymer-based dual-mode biosensor with macrophage-hitchhiking for enhanced tumor imaging and urinalysis. *J. Am. Chem. Soc.* **146**, 33075–33083 (2024).
70. Y. Feng, C. Liu, W. Cui, L. Yang, D. Wu, H. Zhang, X. Wang, Y. Sun, B. He, W. Dai, Q. Zhang, Engineering supramolecular peptide nanofibers for in vivo platelet-hitchhiking beyond ligand-receptor recognition. *Sci. Adv.* **10**, eadq2072 (2024).
71. X. Yu, G. Xing, S. Sheng, L. Jin, Y. Zhang, D. Zhu, L. Mei, X. Dong, F. Lv, Neutrophil camouflaged stealth nanovehicle for photothermal-induced tumor immunotherapy by triggering pyroptosis. *Adv. Sci.* **10**, e2207456 (2023).
72. A. Paschalis, B. Sheehan, R. Riisnaes, D. N. Rodrigues, B. Gurel, C. Bertan, A. Ferreira, M. B. K. Lambros, G. Seed, W. Yuan, D. Dolling, J. C. Welti, A. Neeb, S. Sumanasuriya, P. Rescigno, D. Bianchini, N. Tunariu, S. Carreira, A. Sharp, W. Oyen, J. S. de Bono, Prostate-specific membrane antigen heterogeneity and DNA repair defects in prostate cancer. *Eur. Urol.* **76**, 469–478 (2019).
73. H. Bian, X. Liang, D. Lu, J. Lin, X. Lu, J. Jin, L. Zhang, Y. Wu, H. Chen, W. Zhang, X. Luan, In silico discovery of stapled peptide inhibitor targeting the Nur77-PPARγ interaction and its anti-breast-cancer efficacy. *Adv. Sci.* **11**, e2308435 (2024).
74. M. Tanada, M. Tamiya, A. Matsuo, A. Chiyoda, K. Takano, T. Ito, M. Irie, T. Kotake, R. Takeyama, H. Kawada, R. Hayashi, S. Ishikawa, K. Nomura, N. Furuichi, Y. Morita, M. Kage, S. Hashimoto, K. Nii, H. Sase, K. Ohara, A. Ohta, S. Kuramoto, Y. Nishimura, H. Iikura, T. Shiraishi, Development of orally bioavailable peptides targeting an intracellular protein: From a hit to a Clinical KRAS inhibitor. *J. Am. Chem. Soc.* **145**, 16610–16620 (2023).
75. C. M. Hu, R. H. Fang, J. Copp, B. T. Luk, L. Zhang, A biomimetic nanosponge that absorbs pore-forming toxins. *Nat. Nanotechnol.* **8**, 336–340 (2013).

Acknowledgments: We thank the instrumental support from the Core Facility and Service Center (CFSC) for the School of Life Sciences and Biotechnology (SLSB), Shanghai Jiao Tong University (SJTU), and the Collaborative Center for Industry-Education-Research-Innovation of SLSB, SJTU & Ningbo Yongxin Optics Co. Ltd. **Funding:** This study was supported by National Natural Science Foundation of China (grant no. 82172601 to W.F. and grant nos. 32271437 and 52202180 to X.A.), China Postdoctoral Science Foundation (grant no. 2024M762049 to K.L.), and Natural Science Foundation of Shanghai (grant no. 25ZR1402337 to K.L.), respectively.
Author contributions: Y.L., K.L., Y.D., Haonan Wang, X.A., and W.F. conceived and designed the experiments. Y.L., K.L., Y.D., J.X., Haonan Wang, Huafeng Wang, X.A., and W.F. performed the experiments and analyzed the data. Y.L., K.L., Y.D., S.T.C., Haonan Wang, X.A., and W.F. wrote and revised the manuscript. All authors have approved the final version of the manuscript.
Competing interests: The authors declare that they have no competing interests. **Data and materials availability:** All data needed to evaluate and reproduce the conclusions in the paper are present in the paper and/or the Supplementary Materials.

Submitted 16 July 2025
Accepted 6 November 2025
Published 3 December 2025
10.1126/sciadv.aea6618